Heat flow in vapor dominated areas of the Yellowstone Plateau Volcanic Field: Implications for the thermal budget of the Yellowstone Caldera

Shaul Hurwitz,[1] Robert N. Harris,[2] Cynthia A. Werner,[3] and Fred Murphy[1]

Received 22 May 2012; revised 17 August 2012; accepted 23 August 2012; published 13 October 2012.

[1] Characterizing the vigor of magmatic activity in Yellowstone requires knowledge of the mechanisms and rates of heat transport between magma and the ground surface. We present results from a heat flow study in two vapor dominated, acid-sulfate thermal areas in the Yellowstone Caldera, the 0.11 km^2 Obsidian Pool Thermal Area (OPTA) and the 0.25 km^2 Solfatara Plateau Thermal Area (SPTA). Conductive heat flux through a low permeability layer capping large vapor reservoirs is calculated from soil temperature measurements at >600 locations and from laboratory measurements of soil properties. The conductive heat output is 3.6 ± 0.4 MW and 7.5 ± 0.4 MW from the OPTA and the SPTA, respectively. The advective heat output from soils is 1.3 ± 0.3 MW and 1.2 ± 0.3 MW from the OPTA and the SPTA, respectively and the heat output from thermal pools in the OPTA is 6.8 ± 1.4 MW. These estimates result in a total heat output of 11.8 ± 1.4 MW and 8.8 ± 0.4 MW from OPTA and SPTA, respectively. Focused zones of high heat flux in both thermal areas are roughly aligned with regional faults suggesting that faults in both areas serve as conduits for the rising acid vapor. Extrapolation of the average heat flux from the OPTA (103 ± 2 $W \cdot m^{-2}$) and SPTA (35 ± 3 $W \cdot m^{-2}$) to the ~35 km^2 of vapor dominated areas in Yellowstone yields 3.6 and 1.2 GW, respectively, which is less than the total heat output transported by steam from the Yellowstone Caldera as estimated by the chloride inventory method (4.0 to 8.0 GW).

Citation: Hurwitz, S., R. N. Harris, C. A. Werner, and F. Murphy (2012), Heat flow in vapor dominated areas of the Yellowstone Plateau Volcanic Field: Implications for the thermal budget of the Yellowstone Caldera, *J. Geophys. Res.*, *117*, B10207, doi:10.1029/2012JB009463.

1. Introduction

[2] Three cataclysmic volcanic eruptions occurred in the Yellowstone Plateau Volcanic Field (YPVF) over the past 2.1 million years [*Christiansen*, 2001]. These eruptions represent recent manifestations of a mantle hot spot that has produced a string of large calderas along the Snake River Plain [*Smith and Braile*, 1994; *Pierce and Morgan*, 2009], with the youngest being the 0.64 Ma Yellowstone Caldera (Figure 1). Although the last volcanic eruption in the YPVF occurred over 70,000 years ago, the Yellowstone caldera is currently characterized by extensive seismicity, continuous ground deformation, and considerable heat and mass flux through a large hydrothermal system with over 10,000 thermal features [*Fournier*, 1989; *Lowenstern and Hurwitz*, 2008]. This extensive activity is fueled by a large reservoir of silicic magma in the shallow crust, inferred from seismic velocity anomalies as well as from the shallow depth of the seismogenic zone beneath the caldera [*Husen et al.*, 2004; *Chu et al.*, 2010].

[3] Characterizing the vigor of magmatic activity and forecasting future volcanism in Yellowstone requires knowledge of the mechanisms and rates of heat transport between magma and the ground surface. However, even though Yellowstone is one of Earth's largest and most "restless" calderas [*Newhall and Dzurisin*, 1988; *Lowenstern et al.*, 2006] and its magmatic system is one of the most focused heat sources on Earth, these transport processes and fluxes are poorly constrained. Quantifying heat output from Yellowstone's magmatic system is a daunting task because of the large extent of thermal areas in the Yellowstone Caldera and its surroundings, large-scale phase separation at depth [*White et al.*, 1971; *Fournier*, 1989; *Lowenstern and Hurwitz*, 2008; *Lowenstern et al.*, 2012], and because groundwater flow removes heat and chloride (a proxy for heat) from some areas and concentrates it in others [*Hurwitz et al.*, 2007, 2010].

[4] Vapor dominated thermal areas develop above zones of subsurface steam upflow and are characterized by

[1]U.S. Geological Survey, Menlo Park, California, USA.
[2]College of Oceanic and Atmospheric Sciences, Oregon State University, Corvallis, Oregon, USA.
[3]Alaska Volcano Observatory, U.S. Geological Survey, Anchorage, Alaska, USA.

Corresponding author: S. Hurwitz, U.S. Geological Survey, 345 Middlefield Rd., Menlo Park, CA 94025, USA. (shaulh@usgs.gov)

0148-0227/12/2012JB009463

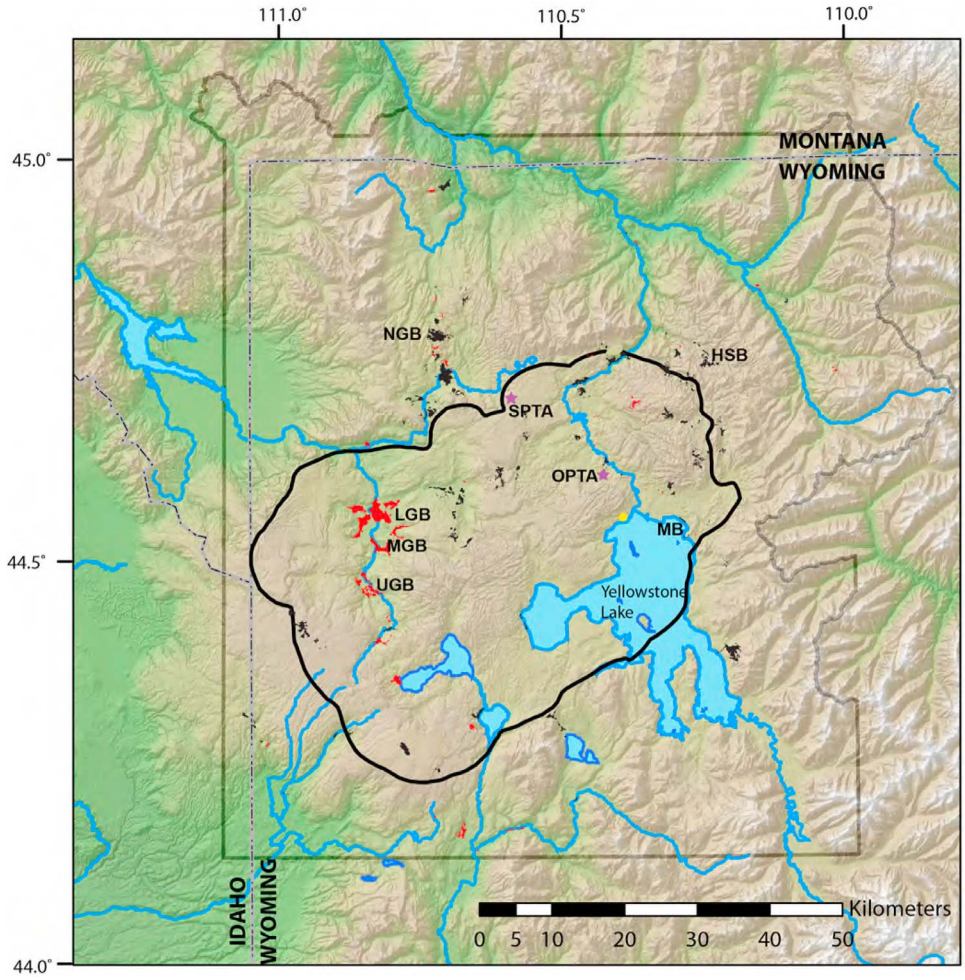

Figure 1. Shaded-relief topography of Yellowstone National Park showing the rim of Yellowstone caldera (solid black line), national park boundary (thick gray line), state boundaries (thin dash-dotted line), neutral-chloride thermal areas (red), and vapor dominated acid-sulfate thermal areas (black) and the major thermal basins in the park; UGB (Upper Geyser Basin), MGB (Midway Geyser Basin), LGB (Lower Geyser Basin), NGB (Norris Geyser Basin), HSB (Hot Spring Basin). Obsidian Pool Thermal Area (OPTA) and Solfatara Plateau Thermal Area (SPTA) are marked with magenta stars. The yellow circle represents the location of the weather station near Yellowstone Lake.

localized and elevated heat flux [*Dawson and Dickinson*, 1970; *White et al.*, 1971; *Sorey and Colvard*, 1994; *Brombach et al.*, 2001; *Chiodini et al.*, 2001; *Hochstein and Bromley*, 2005; *Chiodini et al.*, 2005; *Fridriksson et al.*, 2006; *Werner et al.*, 2006; *Bromley et al.*, 2011]. Within the 2900 km^2 of the Yellowstone caldera there are only ~35 km^2 of vapor dominated, acid-sulfate thermal areas [*Rodman et al.*, 1996; *Werner and Brantley*, 2003], mostly concentrated in the eastern half of the Caldera (Figure 1) where seismic tomography suggests that the silicic magma is shallower than in other parts of the caldera [*Husen et al.*, 2004].

[5] We present results from a field study carried out in June and July, 2010 designed to investigate the mechanisms and quantify the rates of heat transport through two vapor dominated, acid-sulfate areas in the Yellowstone Caldera, the 0.11 km^2 Obsidian Pool Thermal Area (OPTA) (Figure 2) and the 0.25 km^2 Solfatara Plateau Thermal Area (SPTA) (Figure 3). We quantify the magnitudes of the conductive and advective heat flux from soils and the heat flux from thermal pools. The field study is augmented by laboratory measurements of thermal conductivity, porosity, and water saturation. The combined data set allows us to estimate and better understand the relative significance of heat flow from Yellowstone's vapor dominated areas relative to the entire caldera. This understanding has implications for the heat budget of Yellowstone's magmatic system [*Lowenstern and Hurwitz*, 2008] and for monitoring the unique hydrothermal activity in Yellowstone National Park [*Heasler et al.*, 2009].

2. Thermal Budget of the Yellowstone Plateau Volcanic Field

[6] The total heat output from the YPVF is estimated using the chloride inventory method which assumes that all the chloride discharged by rivers draining the YPVF is derived from a single deep parent fluid with a concentration

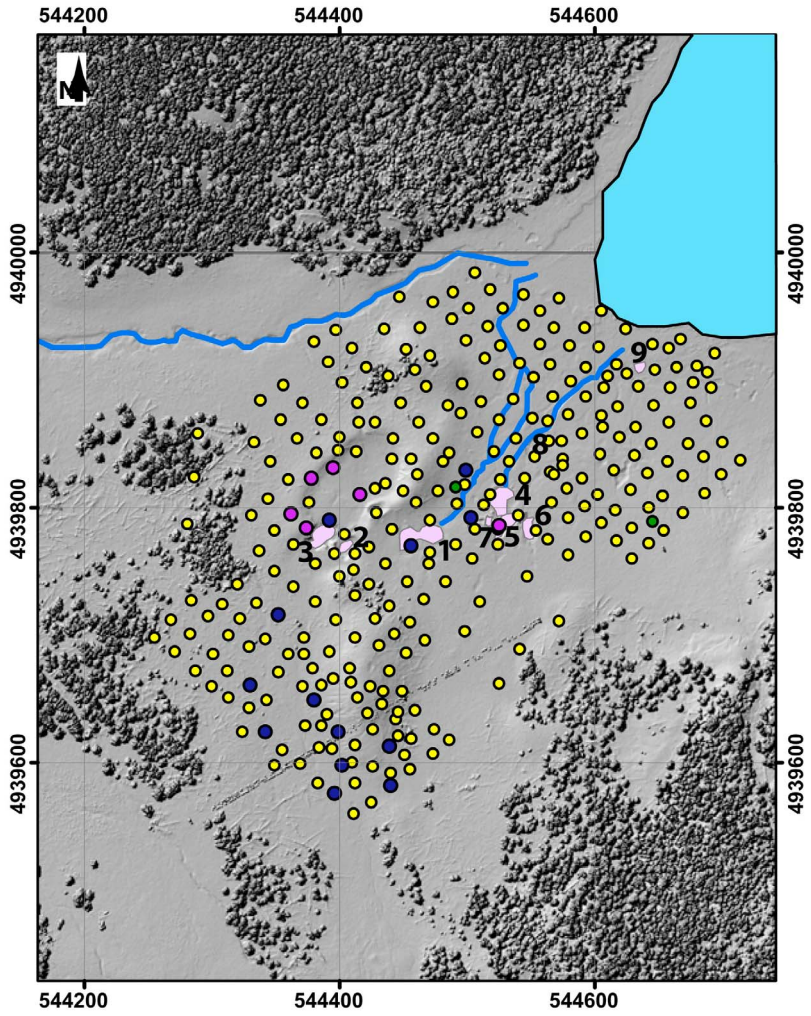

Figure 2. High-resolution shaded-relief topographic map of the Obsidian Pool Thermal Area (OPTA) acquired with airborne LiDAR (www.opentopography.org) showing locations of temperature-depth measurements (yellow circles), thermal pools (shaded pink areas), water vapor flux measurements (blue circles), pits with continuous temperature measurements (green circles), and cores (red circles). The map is projected in the Universal Transverse Mercator (UTM) geographic coordinate system zone 12.

of 400 mg·L^{-1} and a temperature of 340°C (enthalpy of 1,594 kJ·kg^{-1}) [*Fournier et al.*, 1976; *Fournier*, 1979, 1989]. With an average chloride discharge of ~50,000 t·yr^{-1} [*Friedman and Norton*, 2007; *Hurwitz et al.*, 2007, 2010], ~4,000 L·sec^{-1} of parent fluid are discharged. Assuming adiabatic decompression and cooling of the parent fluid from 340°C and 14.6 MPa to 92°C (average boiling temperature in Yellowstone), generates 53 wt% of steam (Figure 4) with an enthalpy of 2,663 kJ·kg^{-1} that transport 5.6 GW of heat to the surface. Liquid water (47 wt%) with an enthalpy of 385 kJ·kg^{-1} transports only 0.7 GW and CO_2 (565 kJ·kg^{-1}) with a flux of 45,000 t·d^{-1} [*Werner and Brantley*, 2003] transports an additional 0.3 GW, for a total heat output from Yellowstone of 6.6 GW. If all this heat is discharged through the 2,900 km^2 of the Yellowstone Caldera (although some heat is discharged outside of the caldera), it corresponds to an average heat flux of 2.3 W·m^{-2}; about 25–40 times greater than that in the neighboring Rocky Mountains [*Blackwell and Richards*, 2004] and that of the average continental crust [*Jaupart and Mareschal*, 2007]. Nevertheless, there are large variations and uncertainties associated with values of the parameters used in these heat output estimates.

[7] Because of the uncertainties associated with parameter values used in the above heat output calculations, and because most of the heat is transported to the ground surface by steam, we calculate plausible end-member scenarios for heat output transported by steam in Yellowstone. An estimated minimum heat output of 4.0 GW corresponds to a chloride concentration of 450 mg·L^{-1}, a temperature of 320°C (1,462 kJ·kg^{-1}), and a chloride flux of 45,000 t·yr^{-1}. In contrast an estimated maximum heat output by steam of 8.0 GW corresponds to a chloride concentration of 350 mg·L^{-1}, a temperature of 360°C (1,762 kJ·kg^{-1}), and a chloride flux of 55,000 t·yr^{-1}. Thus, for a set of plausible parameter values, estimates of heat output from the Yellowstone magmatic system may vary by a factor of two. Our measurements attempt to provide an independent test of these estimates and examine if most of the heat transported by steam in Yellowstone is focused in the ~35 km^2 of acid

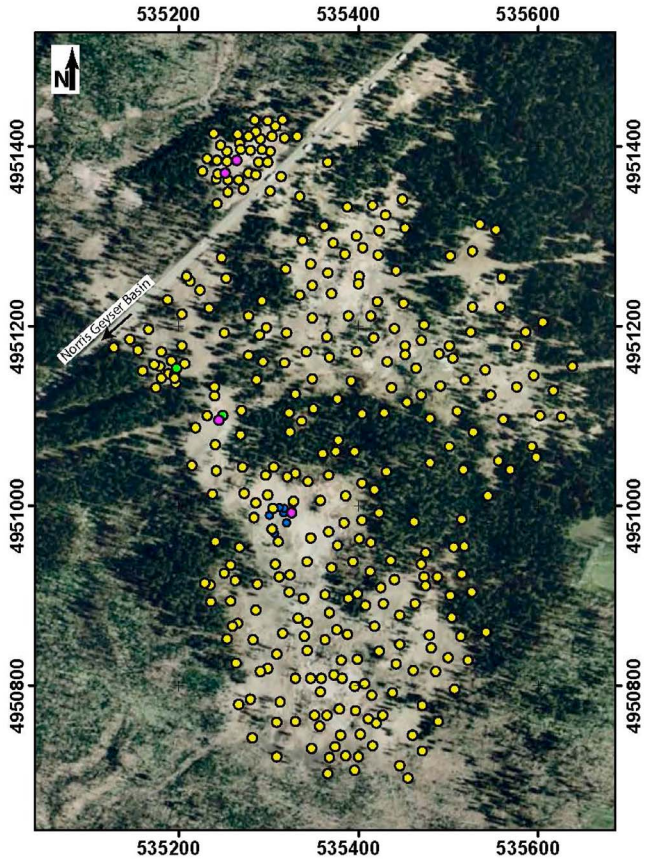

Figure 3. Aerial photograph (Google Earth imagery © Google Inc., used with permission) of the Solfatara Plateau Thermal Area (SPTA) showing locations of temperature-depth measurements (yellow circles) water vapor flux measurements from 2010 (magenta circles) and 2011 (blue circles), and pits with continuous temperature measurements (green circles). The photograph is projected in the Universal Transverse Mercator (UTM) geographic coordinate system zone 12.

sulfate, vapor dominated thermal areas (Figure 1) [*Rodman et al.*, 1996; *Werner and Brantley*, 2003].

3. Geological and Thermal Setting

3.1. Obsidian Pool Thermal Area (OPTA)

[8] The Obsidian Pool Thermal Area (OPTA) (Figure 2) is within the Mud Volcano thermal area, near the intersection of Elephant Back Mountain and the western edge of the Sour Creek Resurgent Dome in the eastern part of the Yellowstone caldera (Figure 1). Within the broader Mud Volcano area, thermal features occur in several isolated areas that consist of cemented glacial deposits and are aligned ~N45°E and ~N45°W [*Christiansen*, 2001]. The Mud Volcano thermal area is characterized by extensive diffuse degassing of CO_2 through soils [*Werner et al.*, 2000; *Werner and Brantley*, 2003] and the highest helium isotope ratio ($^3He/^4He$) measured in Yellowstone [*Werner and Brantley*, 2003; *Bergfeld et al.*, 2011].

[9] The OPTA is surrounded by dense forest and is mostly covered with wild grassland, but the ground is bare around the thermal pools (Figure 2). Based on aerial photos from January 2009, we infer that in winter months snow accumulates along the margins of the thermal area, but not in the center. The OPTA hosts several thermal pools with measured water temperatures between 21.9°C and 84.0°C (Table 1) with mainly acid-sulfate composition and low chloride concentrations [*Shock et al.*, 2005]. All of the pools are bubbling and have temperatures that are below the boiling point of pure water suggesting influx of a CO_2 rich gas. In the northeastern part of the basin, thermal activity in an unnamed lake (Figure 2) cannot be accounted for, but our visual observations in June and July, 2010 suggest it is likely minor. The OPTA drains to Elk Antler Creek, which then drains into the Yellowstone River.

[10] There are several observations that suggest a causal link between current tectonic activity and heat flux variations in the OPTA. The area is close to the area of maximum caldera floor uplift, ~72 cm between 1923 and 1976 [*Pelton and Smith*, 1979]. Beginning in May 1978, a 7 month seismic swarm was centered below and adjacent to OPTA with hypocenter depths ranging between ~1 and 5 km [*Pitt and Hutchinson*, 1982]. Clear signs of increased heat output followed the seismic swarm including increased soil temperature, increase in CO_2 emissions, tree mortality, and the generation of new mud pots and fumaroles in the main Mud Volcano thermal area about 1 km NW of the OPTA [*Pitt and Hutchinson*, 1982; *Evans et al.*, 2010]. Hydrothermal activity then began to decline and returned to pre-1978 levels during the winter of 1979–1980. Analysis of aerial photos covering the area around the OPTA for the period between 1954 and 2009 indicates an apparent increase of the thermal area and significant changes in the areas of thermal pools. A new mud pot (pool 7 in Figure S1 in the auxiliary material) formed sometime between October 2006 and April 2007 and significant changes in the morphology of the southwest area

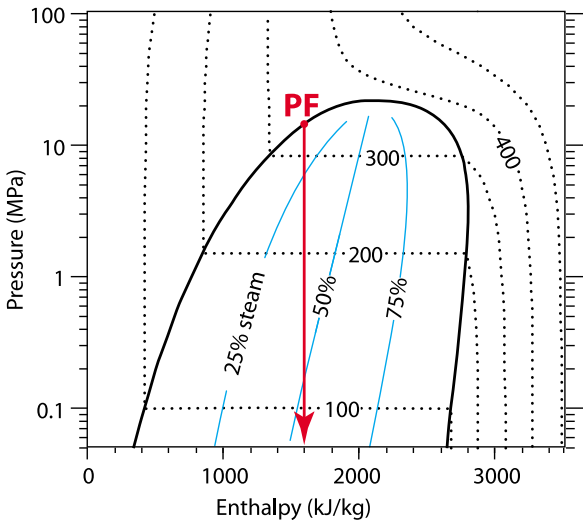

Figure 4. Pressure-enthalpy diagram for pure water showing contours of equal temperature (dashed line) and mass fraction of steam (solid line) within the two-phase region (bounded by thick solid line). The vertical red line represents adiabatic decompression and cooling of Yellowstone's parent fluid (PF) that generates 53 wt% steam at the ground surface.

Table 1. Heat Output From Pools in the Obsidian Pool Thermal Area (OPTA)[a]

Pool	Easting	Northing	Area (m^2)	Temp (°C)	H_{EVAP} (MW)	H_{RAD} (MW)	H_{COND} (MW)	Total (MW)
1	544461	4939778	495	59.8	1.5	0.3	0.2	2.0
2	544404	4939770	66	48.1	0.1	0.0	0.0	0.2
3	544385	4939777	136	80.9	1.3	0.1	0.1	1.5
4	544526	4939804	300	63.7	1.1	0.2	0.2	1.5
5	544528	4939786	124	73.0	0.8	0.1	0.1	1.0
6	544549	4939785	224	25.7	0.1	0.1	0.0	0.2
7	544517	4939790	4	79.8	0.0	0.0	0.0	0.0
8	544549	4939853	25	66.0	0.1	0.0	0.0	0.1
9	544636	4939910	60	62.1	0.2	0.0	0.0	0.3
Total			1434		5.2	0.9	0.7	6.8

[a]Constants used in the calculations: T_{air} (air temperature) = 10.7°C; Pa (air pressure) = 760 mbar; W (wind speed) = 1.9 $m \cdot s^{-1}$; ε (emissivity) = 0.98; σ (Stephan Boltzman constant) = $5.67 \cdot 10^{-8}$ $W \cdot m^{-2} \cdot K^{-4}$; c (Bowen constant) = 0.61 $m \cdot K^{-1}$.

since 1999 (J. Spear, Colorado School of Mines, written communication, January 2012) also suggests that the thermal state of the area is transient.[1]

3.2. Solfatara Plateau Thermal Area (SPTA)

[11] The Solfatara Plateau Thermal Area (SPTA) (Figure 3) lies on the northern boundary of Yellowstone Caldera (Figure 1), near the center of the north rim uplift anomaly [*Wicks et al.*, 2006] where InSAR and GPS data reveal large vertical displacements relative to the Yellowstone Caldera since 1996 [*Wicks et al.*, 2006; *Chang et al.*, 2007]. The lithology consists of cemented glacial deposits surrounded by the 110 ± 3 ka Solfatara Plateau flow. Faults to the north of the SPTA and the northern caldera boundary trend NNW [*Christiansen*, 2001]. A M_L 6.1 Earthquake occurred ~5.7 km to the SW of SPTA on June 30, 1975, with a focal mechanism indicating normal faulting along a NNW strike [*Pitt et al.*, 1979], parallel to the faults north and south of the SPTA.

[12] During our 2010 survey no pools or creeks were observed in SPTA. Several small fumaroles with visible native sulfur deposits were mainly focused in a small area north of the Norris to Canyon road (Figure 3) and in a small area in the western part of the basin south of the Norris to Canyon road. Aerial photos indicate that the forested area surrounding the thermal basin grew larger and denser between 1954 and 2009, suggesting an overall decline in thermal activity.

4. Heat Flux From Vapor Dominated Areas

[13] Conceptual models of heat transport in vapor dominated areas suggest that rising steam and non-condensable gases, mainly CO_2 and H_2S fill open fractures throughout a significant vertical extent beneath a thin low permeability cap layer consisting mainly of clay minerals [*White et al.*, 1971; *Hochstein and Bromley*, 2005]. Heat is transferred by the rising vapor to the base of the cap layer, where the vapor condenses and the liquid descends down the fractures ("heat pipe"). In this conceptual model (Figure 5), heat transport across the low permeability layer is dominated by conduction, but where the cap layer is fractured heat discharges advectively through fumaroles or vapor condenses into pools. In the upper part of the low permeability cap layer, the temperature gradient is disturbed by variations in air temperature and solar insolation such that temperatures increase nonlinearly with depth. However, because background thermal gradients in the low permeability layer are

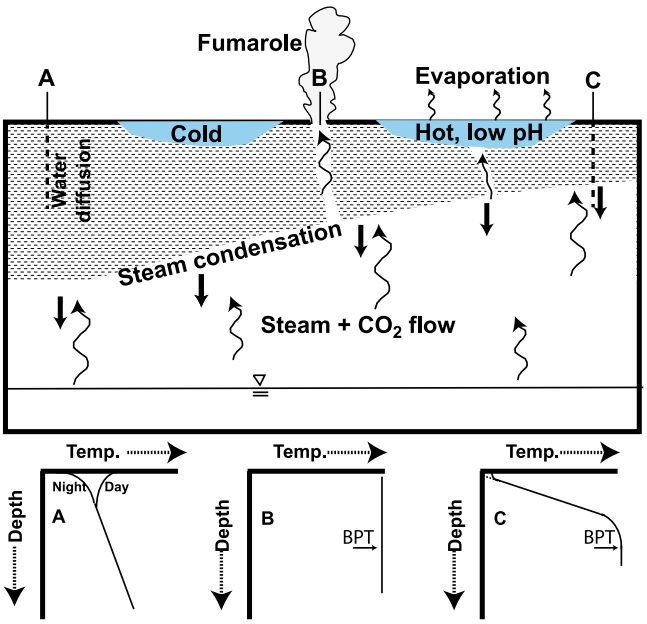

Figure 5. A schematic illustration showing modes of heat transport in vapor dominated areas and the resulting temperature gradients (modified after *Hochstein and Bromley* [2005]). In areas with a relatively thick low permeability, clay-rich caprock (indicated by A) temperature gradients are moderate and vary considerably in response to air temperature and solar insolation fluctuations. In areas where a fracture transects the entire caprock and connects the vapor dominated area with the ground surface (indicated by B), a fumarole will form with fluid discharge at boiling temperature (BPT). Areas with a thin caprock (indicated by C) are characterized by a large temperature gradient and variations in response to air temperature and solar insolation fluctuations are small. When steam condenses into a pool (as the one on the right) it will be hot and acid. In contrast, a pool that is not connected to the vapor dominated area will remain cold and its waters will be neutral. Below the caprock rising steam and non-condensable gases (curved thin lines) fill open fractures and the vapor condensate (thick lines) descends down the fractured rocks.

[1]Auxiliary materials are available in the HTML. doi:10.1029/2012JB009463.

generally large, the variations in subsurface temperature due to surface air temperature and solar insolation variations are a relatively small component of the total thermal gradient (profile C in Figure 5).

[14] The total heat flux q_{tot} ($W \cdot m^{-2}$) measured at the surface of these vapor dominated areas can be expressed as,

$$q_{tot} = q_{soil} + q_{pool}, \quad (1)$$

where q_{soil} is the heat flux through the soil and q_{pool} is the heat flux from pools. Heat flux through soils can be expressed as,

$$q_{soil} = q_{cond} + q_{adv}, \quad (2)$$

where the conductive heat flux (q_{cond}) is expressed by Fourier's law,

$$q_{cond} = K\left(\frac{dT}{dz}\right), \quad (3)$$

where K ($W \cdot m^{-1} \cdot K^{-1}$) is the bulk thermal conductivity (composite of the rock and the pore fluid thermal conductivities), T is temperature, and z is depth. Advective heat transport by water vapor in partially saturated soils is controlled by vapor concentration gradients and temperature gradients [*Parlange et al.*, 1998; *Heitman et al.*, 2008; *Bittelli et al.*, 2008] and is described by,

$$q_{adv} = \rho_v \cdot L \cdot Q_v, \quad (4)$$

where ρ_v ($kg \cdot m^{-3}$) is vapor density, L is the latent heat of vaporization ($\sim$2,270 $kJ \cdot kg^{-1}$), and Q_v ($m \cdot s^{-1}$) is the vapor flow rate. The heat flux from the surface of an enclosed pool (q_{pool}) with no surface water inflow or outflow can be expressed as,

$$q_{pool} = q_{evapw} + q_{radw} + q_{condw}, \quad (5)$$

where q_{evapw}, q_{radw}, and q_{condw}, are the evaporative, radiative, and conductive heat fluxes from the pool, respectively.

[15] Evaporative heat flux from the pool is driven by a vapor-pressure difference between the pool and the atmosphere and can be expressed by [*Adams et al.*, 1990; *Pasternack and Varekamp*, 1997; *Fournier et al.*, 2009],

$$q_{evapw} = \left[\left[2.7(T_{wv} - T_{av})^{1/3}\right]^2 + \left[5.1(A/10000)^{-0.05} W\right]^2\right]^{1/2} \cdot (e_w - e_a)A, \quad (6)$$

where W is the wind speed ($m \cdot s^{-1}$), A is the surface area of the pool (m^2), and T_{wv} and T_{av} (K) are the virtual air temperatures for the lake water and ambient air, respectively, defined as,

$$T_v = \frac{T}{1 - 0.378e/P}, \quad (7)$$

where P is the barometric pressure (mbar) and e_w and e_a are the saturated water and atmospheric vapor pressures at the pool and air temperatures, respectively calculated using a polynomial fit to data from the NBS/NRC steam tables [*Haar et al.*, 1984],

$$e = 9.667 \cdot 10^{-6}T^4 - 1.091 \cdot 10^{-2}T^3 + 4.648 \cdot T^2 - 8.856 \cdot 10^2 T + 6.360 \cdot 10^4, \quad (8)$$

Radiative heat loss from a water surface is given by,

$$q_{radw} = A \cdot \varepsilon \cdot \sigma \cdot T_w^4, \quad (9)$$

where ε is the emissivity of a smooth surface (0.98), σ is the Stefan-Boltzmann constant - $5.67 \cdot 10^{-8}$ $W \cdot m^{-2} \cdot K^{-4}$ (U.S. National Institute of Standards and Technology - http://physics.nist.gov/cgi-bin/cuu/Value?sigma), and T_w is the absolute temperature of the water surface (K). Conductive heat loss is related to the evaporative heat loss through the Bowen constant (0.61 $m \cdot K^{-1}$), and is driven by the temperature gradient between the water surface, T_w and air, T_a [*Brown et al.*, 1991],

$$q_{condw} = 0.61\frac{T_w - T_a}{e_w - e_a} q_{evap}. \quad (10)$$

The total heat output (MW) from a vapor dominated area is given by:

$$\dot{Q}_{total} = \dot{Q}_{cond} + \dot{Q}_{adv} + \dot{Q}_{pool}. \quad (11)$$

5. Methods

5.1. Temperature Gradient Measurements and Analysis

[16] Temperature-depth measurements were made at 299 locations in the OPTA (Figure 2) and at 324 locations in the SPTA (Figure 3). At each measurement location four holes were made in the ground separated by <10 cm, using a 3/8 inch (0.95 cm) steel rod driven with a hammer, and thermocouple probes were then inserted into the holes (Figure 6). Each probe was constructed from 3/8 inch (0.95 cm) stainless steel tube, and contained four type K thermocouple sensors. With four probes, a total of 16 thermocouples were used at each measuring location (Figure 6a). The sensors with a precision of 0.1°C were calibrated in water baths against National Institute Standards and Technology (NIST) traceable glass thermometers between 10°C and 80°C and all read within 0.5°C of the glass thermometers. Each of the probes was inserted in its respective hole allowing the 16 sensors to be aligned at designated depths that ranged from 5 to 100 cm. We estimate the actual depth accuracy to be <2 cm, due to uneven ground. In a few cases hard ground prevented the complete insertion of probes and temperatures at shallower depths were measured. Each thermocouple sensor was connected to a data logger and sampled at a 2 s interval for periods ranging from 8 to 15 min after insertion to ensure near thermal equilibrium. The equilibrium temperature and the standard deviations for each sensor were calculated over the last 80 s corresponding to 40 samples. In general linear trends to the time series are <0.0002°C·sec^{-1} over the 80 s fitting interval.

[17] During the field experiment we monitored diurnal temperature variations at each thermal area. Diurnal

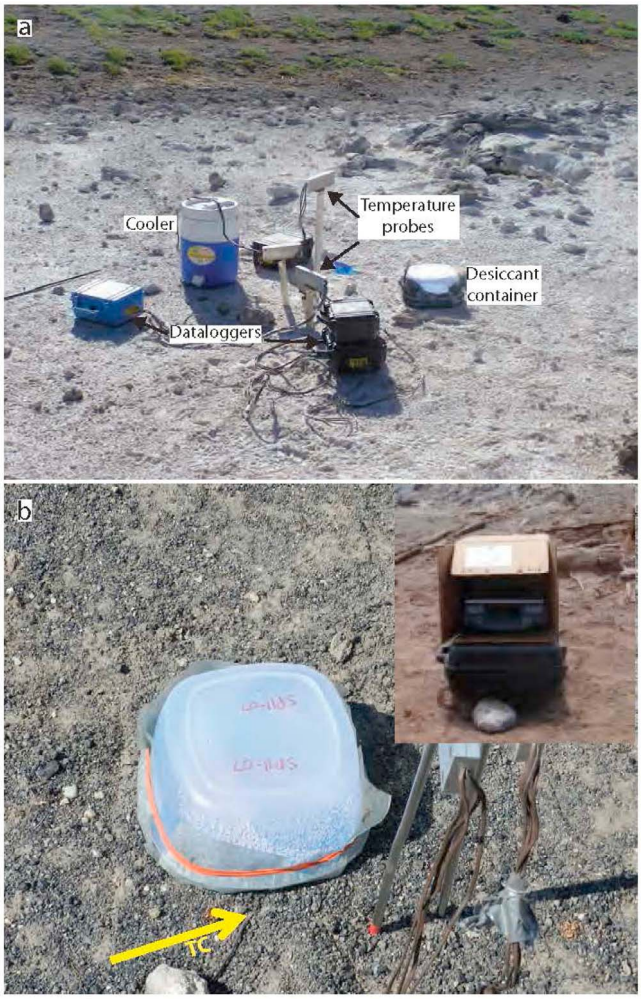

Figure 6. Photos showing (a) setup for the temperature-depth measurements, including the temperature probes and the data loggers, and (b) setup for the vapor flux experiment. The inverted container with 8-mesh Drierite® desiccant is covered with a PVC-coated polyester screen. The yellow arrow points to the thermocouple wire (TC) inserted between the inverted container and the ground surface. The photo in the inset shows the portable scale used to weigh the desiccant.

temperature corrections are based on thermistors (HOBO® U23 Pro v2 2x) buried at depths of 5, 10, 15, 20, 25, and 35 cm in two pits in OPTA and two pits in SPTA (Figures 2 and 3) for the six-week duration of the experiment. Temperature measurements were recorded at a 5-min intervals and display diurnal and weekly variations (Figure 7a). Diurnal temperature variations decreased with depth consistent with conductive heat transfer. As an example, temperatures varied by 22.4°C, 4.5°C and 1.2°C at depths of 5 cm, 20 cm, and 35 cm, respectively at site OPIT1 on June 27, 2010 (Figure 7b).

[18] For each pit we parameterized the shallowest temperature measurements in terms of a series of n step functions of amplitude ΔT_i and inverted for the thermal diffusivity that best matches the temperatures measured at greater depths using [*Carslaw and Jaeger*, 1959],

$$T(z,t) = \sum_{i=1}^{n} \Delta T_i erfc\left(\frac{z}{\sqrt{4\alpha\tau}}\right), \tag{12}$$

where T is temperature, z is depth, t is time, *erfc* is the complementary error function, τ is time before present and α is thermal diffusivity. Model fits to the deeper time series are generally good (Figure 7c) and the best fitting thermal diffusivity is well determined. Although there is some indication that thermal diffusivity increases slightly with depth we use a constant value of $1{\cdot}10^{-6}$ $m^2{\cdot}s^{-1}$ based on the fit to the deepest thermistor. The calculated thermal diffusivity was used to remove the diurnal variation from our observed equilibrium temperatures assuming the 5 cm temperature series in OPIT1 and SPIT1 are representative of the OPTA and SPTA, respectively. The range in the diurnal gradients over the period of the experiment at both sites is approximately $6°C{\cdot}m^{-1}$. Because our soil temperature measurements were made during the day when the previous night's thermal signal had penetrated to the measuring depth, diurnal corrections decreased the observed gradients. The analytical uncertainties of the corrected thermal gradients are computed using standard formulas [*Bevington*, 1969].

[19] Equilibrium temperatures determined from the 16 sensors, the temperature gradients, and the ground surface temperature extrapolated from the temperature gradients, are given in Tables S1 and S2 in the auxiliary material for the OPTA and the SPTA, respectively. For profiles with a maximum temperature <60°C the linear fit is based on the seven bottom most corrected temperatures in the profiles (50–100 cm), whereas for profiles with maximum temperatures >60°C, the linear fit is based on a minimum of four temperature measurements within the upper 35 cm of the corrected profiles.

5.2. Thermal Conductivity Measurements and Analysis

[20] Matrix thermal conductivity, porosity, and water saturation were determined on core samples obtained from the OPTA using either a 3.24 cm or 2.11 cm diameter cylindrical steel corer. These core samples were immediately wrapped in aluminum foil and placed in a cooler. In the laboratory, long cores were split into smaller pieces for measurement. In addition, five shallow (<10 cm) soil samples were collected in the OPTA in September 2008 for matrix thermal conductivity measurements.

[21] Matrix thermal conductivities were measured on a total of 50 samples from the OPTA using a divided bar apparatus at the U.S Geological Survey heat flow laboratory [*Sass et al.*, 1984]. The unconsolidated soil was placed in a cell and saturated with water under vacuum. Thermal conductivity was computed by subjecting the cell to a known heat flow and measuring the temperatures at the top and bottom of the cell. Grain thermal conductivity was computed as the ratio of the heat flow to the thermal gradient through the cell and adjusted for the thermal conductivity of water within the pore space. The measurement error is typically within 5% [*Sass et al.*, 1984]. The average matrix thermal conductivity of the 50 samples is 1.95 ± 0.22 $W{\cdot}m^{-1}{\cdot}K^{-1}$ (Table S3).

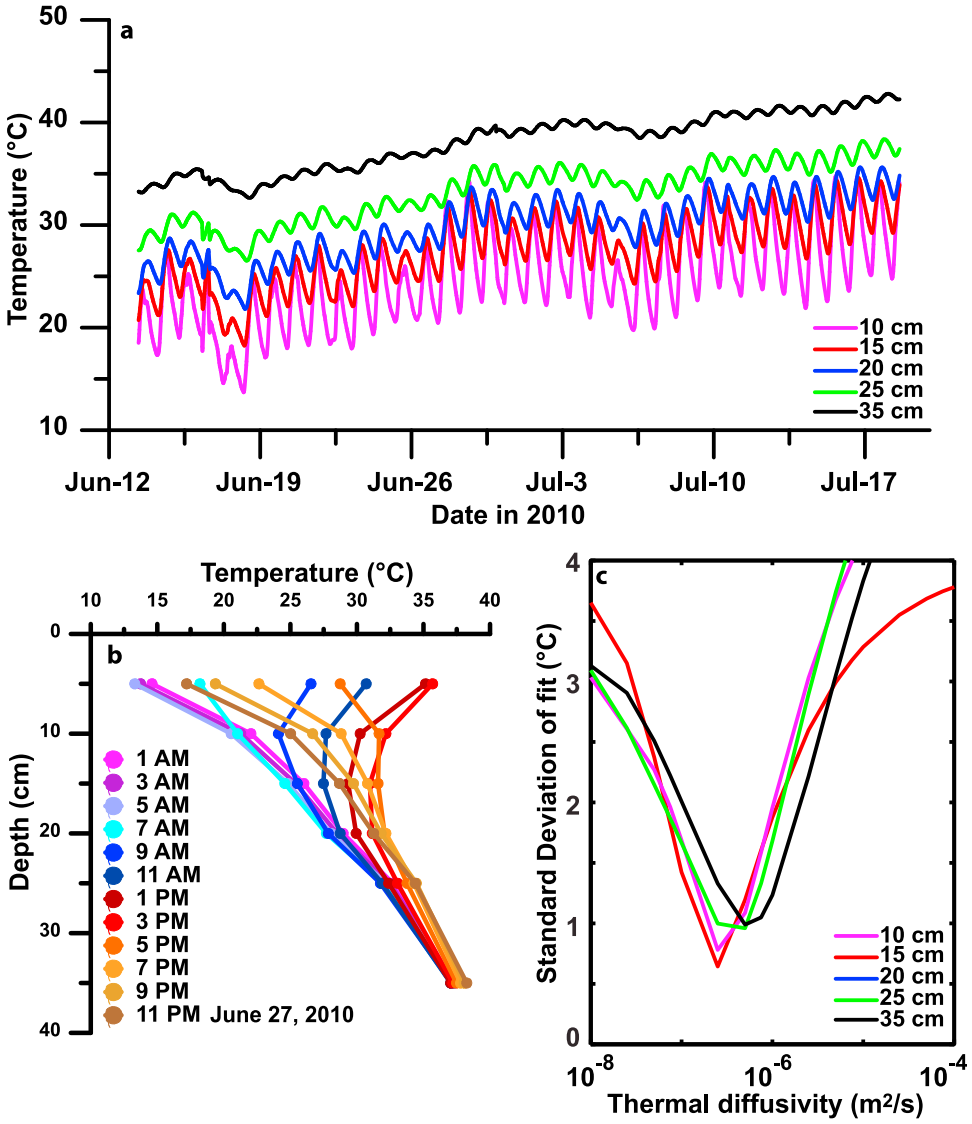

Figure 7. (a) Observed temperature-time series at various depths in OPIT1 (Figure 2), (b) temperature variations in OPIT1 on 27 June, 2010, and (c) standard deviation of model fit to depths based on time series at 5 cm depth in OPIT1 as a function of thermal diffusivity. The best fitting thermal diffusivity corresponds to minimum standard deviation and is approximately $1{\cdot}10^{-6}$ m^2/s.

[22] Porosity and water saturation measurements were made on core samples from subsurface depths >30 cm to represent the depth range for which most temperature gradients were determined. A total of 13 samples from 8 separate cores were analyzed at the U.S Geological Survey laboratory in Menlo Park, CA. Samples were weighed and then oven-dried at a temperature of 105°C for 24 h and then re-weighed to determine the mass of evaporated water. When the samples were heated in the oven, a strong odor appeared, indicating that some samples contained significant amount of organic volatiles and/or sulfur-rich gas. Sample porosity (n) was calculated by,

$$n = 1 - \frac{\rho_b}{\rho_s}, \tag{13}$$

where ρ_b is the bulk core density and ρ_s is the solid phase density assumed to be 2,650 kg/m^3, representing a illite-montmorillonite soil. Bulk core density was calculated by,

$$\rho_b = \frac{m_s}{V_b}, \tag{14}$$

where m_s is the mass of the dry solid phase and V_b is the volume of the core. Effects of compression during core recovery were ignored. Volumetric water saturation (S) was calculated by,

$$S = \frac{V_l}{V_b}, \tag{15}$$

where V_l is the volume of liquid water released during dehydration in the oven assuming water density to be 1,000 kg/m^3. The average porosity and volumetric water

Table 2. Results From Water Vapor Flux Measurements

Station	Easting	Northing	Duration (hh:mm:ss)	Vapor Flux ($g*hr^{-1}*m^{-2}$)	STD	q_{adv} ($W \cdot m^{-2}$)	Temp. Grad. ($°C*m^{-1}$)	BHT[a] (°C)	q_{cond} ($W \cdot m^{-2}$)	$\%q_{adv}$[b]
OBS145	544395	4939831	4:29:20	287	87	181	292	90.94	380	32
OBS146	544416	4939810	4:01:40	148	39	93	258	90.63	335	22
OBS172	544374	4939784	4:08:40	95	15	60	44	72.86[c]	57	51
OBS173	544362	4939795	4:02:11	132	37	83	28	41.57	37	69
OBS283	544378	4939823	3:59:00	147	47	93	17	35.45	23	80
OBS336	544524	4939783	5:51:00	153	–	96	32	51.29	42	70
SFT011	535265	4951384	3:00:00	189	36	119	37	56.87	48	71
SFT012	535252	4951370	31:13:05	59	15	37	96	79.50	125	23
SFT070	535326	4950992	30:06:30	69	34	44	131	88.11[c]	170	20
SFT093	535245	4951095	30:29:45	43	11	27	38	78.76	49	35
SP11-01	535327	4951002	7:37:00	146	34	92				
SP11-02	535317	4950992	7:43:00	136	16	86	393	92.06[c]	511	14
SP11-03	535318	4950997	7:31:00	173	52	109				
SP11-04	535301	4950989	7:27:00	73	20	46				
SP11-05	535320	4950981	7:18:00	103	25	65				
SP11-06[c]	535312	4950998	4:20:00	248		156	400		520	23
SP11-07	535307	4950969	7:08:00	121	11	76	79	91.90[c]	103	43
Average				137	32	86				
Average without overnight experiments				154	35	97				

[a]BHT, bottom hole temperature.
[b]Percentage from q_{soil}.
[c]Extrapolated bottom hole temperature.

fraction of the core samples are 0.39 ± 0.09 and 0.38 ± 0.11, respectively (Table S4 in the auxiliary material).

[23] There are several models used to calculate the bulk thermal conductivity (K_b) of porous and variably saturated rocks [*Jorand et al.*, 2011]. The geometric mean bulk thermal conductivity is applicable only when the constituent conductivities vary by less than one order of magnitude [*Sass et al.*, 1971] and is applicable mainly in rocks with water saturation >60% [*Jorand et al.*, 2011]. Neither of these conditions is applicable to our samples. A geometric mean model results in an unrealistically low bulk thermal conductivity of 0.61 ± 0.23 $W \cdot m^{-1} \cdot K^{-1}$. The arithmetic mean bulk thermal conductivity represents the volumetric fraction of each phase (solid, liquid and gas) multiplied by the phase thermal conductivity and is defined by,

$$K_b = X_s \cdot K_s + X_l \cdot K_l + X_g \cdot K_g, \tag{16}$$

and the harmonic mean bulk thermal conductivity is defined by,

$$K_b = \left[\frac{X_s}{K_s} + \frac{X_l}{K_l} + \frac{X_g}{K_g}\right]^{-1}, \tag{17}$$

where X is the volume fraction of each phase and the subscripts s, l, and g are for solid, liquid, and gas, respectively. We assume that the thermal conductivity of void volume not containing liquid water (K_l = 0.67 $W \cdot m^{-1} \cdot K^{-1}$) represents an average with equal amounts of carbon-dioxide, nitrogen, and methane (K_g = 0.03 $W \cdot m^{-1} \cdot K^{-1}$) calculated using the NIST database of thermophysical properties of fluids (http://webbook.nist.gov/chemistry/fluid/). The calculated arithmetic mean and harmonic mean bulk thermal conductivities (K_b) are 1.30 ± 0.21 $W \cdot m^{-1} \cdot K^{-1}$ and 1.24 ± 0.20 $W \cdot m^{-1} \cdot K^{-1}$, respectively. Following the approach of *Jorand et al.* [2011] we calculate a arithmetic-harmonic mean of 1.27 ± 0.21 $W \cdot m^{-1} \cdot K^{-1}$, which is an average of the two means. The cumulative uncertainties were calculated by propagating the errors resulting from averaging matrix thermal conductivity, porosity, and volumetric water saturation.

5.3. Measurements of Water Flux Through Soils

[24] We carried out experiments to measure water vapor flux in the OPTA in September 2010 and in the SPTA in September 2010 and September 2011. As an alternative approach to the water calorimeter method [*Hochstein and Bromley*, 2005] we developed a novel method to measure water flux from the soil. We used weighed polyethylene containers with an open area of 0.042 m^2 that were filled with an anhydrite desiccant (Drierite®) (Figure 6b), and reweighed periodically with a calibrated portable scale (Ohaus EB15® Bench Scale) with a resolution of 0.5 g. The containers with the desiccant were then covered with a PVC-coated polyester screen and inverted, so that the screen was in contact with the soil. We used desiccant grains because in contrast to the calorimeter, they are permeable and allow for undisturbed flow of the water vapor into the atmosphere. Drierite® (anhydrite) was chosen because it can absorb up to 8 wt% water before saturation, but it does not absorb CO_2 which is known to be emitted from soils at high rates in both thermal areas. To calculate the heat transported with the vapor absorbed on the desiccant, equation (4) can be reformulated as,

$$q_{adv} = L \cdot \frac{\frac{dm}{dt}}{A}, \tag{18}$$

where dm/dt is the time-dependent mass of water absorbed by the desiccant and A (m^2) is the open area of the container.

[25] A total of 6 experiments were carried out in the OPTA mainly in the western part (Figure 2) where temperature gradients are mostly high. Four experiments were carried out

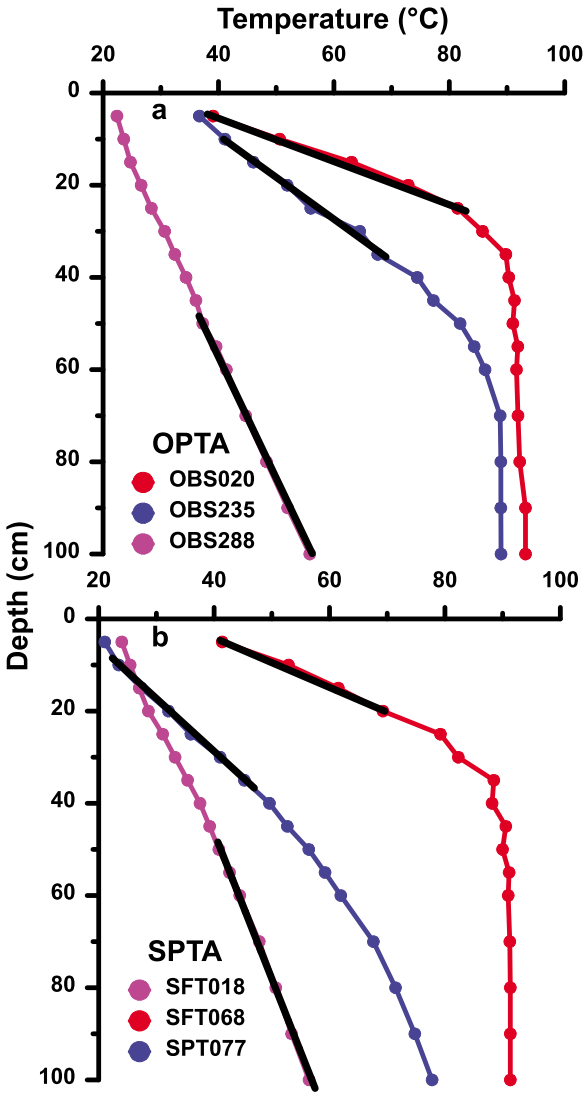

Figure 8. Representative temperature depth profiles at (a) Obsidian Pool Thermal Area (OPTA) and (b) Solfatara Plateau Thermal area (SPTA). Small circles show equilibrium temperatures of individual sensors and the black lines show the calculated temperature gradient. In profiles with bottom hole temperatures <60.0°C the gradient was calculated from the 7 bottommost temperatures, for bottom hole temperatures between 60.0°C and 80.0°C, gradients were mostly determined from the temperatures of sensors 2–7 (counting from the top), and for bottom hole temperatures >80.0°C, gradients were typically determined from the temperatures of the 4 uppermost sensors. Note the bottommost isothermal section of profile OBS235 which is below the boiling point of pure water for the elevation of the OPTA. This is a consequence of dissolved carbon dioxide depressing the boiling point of the water.

in the SPTA in 2010 and seven additional experiments were conducted in 2011, all in areas with high temperature gradients (Figure 3). The duration of the experiments ranged from 3 to 31 h (Table 2). For the shorter experiments, the containers were lifted from the ground at intervals ranging from 30 to 60 min and re-weighed to measure the mass of water that was absorbed by the desiccant. For the overnight experiments, the containers were measured at 30 to 60 min intervals on the first day and once more in the following morning. Every time the container was removed from the ground for weighing, it was shaken, to avoid accumulation of hydrated grains in the layer closest to the ground. In experiments SP11–02 and SP11–07 (Table 2) a thermocouple wire was inserted between the polyester screen and the ground surface to measure the time varying temperature of the ascending vapor.

5.4. Measurements of Heat Flux From Pools

[26] Temperature measurements were made with a thermistor probe (±0.1°C) in nine pools (Figure S1 in the auxiliary material) within the OPTA (Figure 2) in September 2010. There were no pools in the SPTA in 2010 or 2011. At each pool temperature measurements were made at various locations and depths and the highest temperature at each depth was recorded. The surface area of each pool (Table 1) was measured with a measuring tape and was then also calculated by tracing the pool outline on the high resolution, airborne LiDAR digital elevation model (Figure 2). The discrepancy between the two measurements is <10%. Surface temperature measurements along the shores of the unnamed lake at the NW part of the basin (Figure 2) were made at only a few locations and generally correlated with air temperature. Wind speed and air temperature values required for solving equation (6) are based on average hourly data from June and July 2010 obtained from the National Climatic Data Center (http://www.ncdc.noaa.gov/oa/ncdc.html) weather station at Yellowstone Lake, WY (COOP ID 485345) located 7.5 km away from the OPTA (Figure 1).

6. Results

6.1. Conductive Heat Flux

[27] Representative temperature-depth profiles are shown in Figure 8; profiles with bottom hole temperatures <60°C are typically approximately linear after corrections for diurnal variations as in OBS288 (Figure 8a) and SFT 108 (Figure 8b). When boiling temperature is within 1 m from the ground surface, profiles are typically isothermal at the boiling temperature in the lower part and contain a large temperature gradient in the upper part as in OBS020 and OBS235 (Figure 8a) and SFT068 (Figure 8b). Although a few profiles show abrupt changes, probably resulting from small errors in depth measurements, most nonlinearities are gradual and systematic suggesting that instrumental noise is insignificant. Inaccurate corrections for diurnal temperature variations introduce relatively small perturbations to the large background gradients. From the 299 measurements made at the OPTA, 12 temperature gradients are negative (likely reflecting measurement errors or inaccurate diurnal corrections) and are omitted from further calculations, 126 gradients range between 0 and 10°C·m^{-1}, and 24 gradients are >100°C·m^{-1}. In SPTA, 110 temperature gradients are <10°C·m^{-1} and only 9 gradients are >100°C·m^{-1} (Figures 9a and 9b).

[28] Boiling within the upper 1 m of the subsurface is associated with significant nonlinearities in the temperature

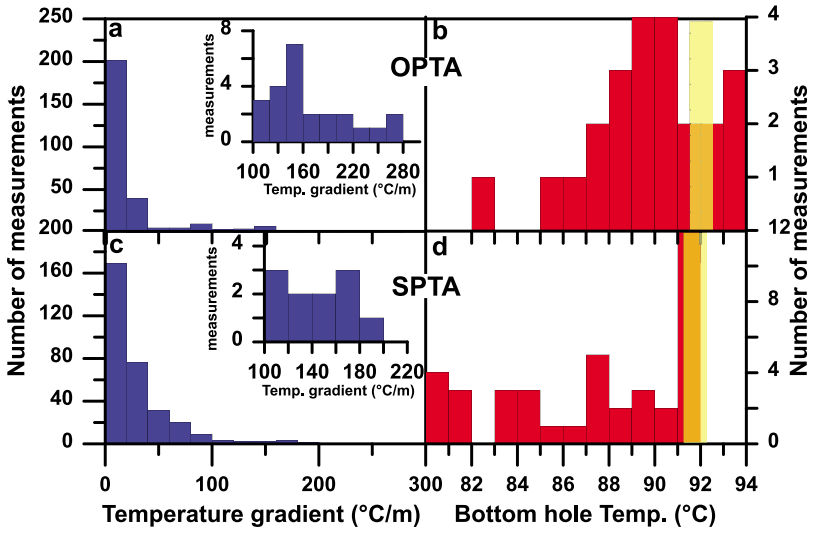

Figure 9. Histograms of (a) temperature gradients (20°C·m^{-1} bins) at the Obsidian Pool Thermal Area (OPTA) with gradients >100°C·m^{-1} shown in the inset, (b) bottom hole temperatures >80°C at the Obsidian Pool Thermal Area (OPTA), (c) temperature gradients at the Solfatara Plateau Thermal Area (SPTA), and (d) bottom hole temperatures >80°C at the Solfatara Plateau Thermal Area (SPTA). The shaded yellow area represents the range of boiling temperatures for the period when this study was carried out in June and July, 2010.

profiles. Several measurements in both the OPTA and the SPTA reached the boiling temperature for the respective elevation of the thermal area. The boiling temperature of pure water for the duration of our measurements (June 9 to July 19, 2010) was calculated using barometric pressure data from a meteorological station 7 km to the south of the OPTA near Yellowstone Lake (Figure 1) and the NIST database of thermophysical properties (http://webbook.nist.gov/chemistry/fluid/). Boiling temperatures varied between 91.6 and 92.5°C at the OPTA (elevation of ~2400 m) and between 91.3 and 92.2°C at the SPTA (~2480 m) (Figures 9c and 9d). At the SPTA bottom hole temperatures >91°C were measured at 12 locations (Figure 9d) and in 9 of these locations the temperature gradient between depths of 100 cm and 80 cm was less than 1°C·m^{-1} and in five locations the temperature gradient between depths of 100 cm and 50 cm is <1°C·m^{-1}, suggesting advective heat transport. At some of these locations, when the probes were pulled out of the ground, water emerged from the surface indicating we had inadvertently penetrated the clay cap. At the OPTA seven bottom hole temperatures were above the boiling temperatures of pure water (Figure 9c). At several other locations near-isothermal temperatures ranging from 88.4°C (OBS207) to 91.0°C (OBS229) extend from a depth of 100 cm up to 30 cm (OBS277). These temperatures suggest boiling of a CO_2-H_2O mixture, consistent with the high CO_2 diffuse fluxes measured in the area [*Werner et al.*, 2000] and with the high concentrations of CO_2 in fumaroles and thermal pools [*Bergfeld et al.*, 2011].

[29] Best fitting surface temperature intercepts determined from the temperature-depth measurements have a mean and standard deviation of 13.3 ± 4.7°C and 23.4 ± 7.7°C at OPTA and SPTA, respectively. These values are above the average air temperature for June and July 2010 (11°C) at the Yellowstone Lake weather station (Figure 1), but ground temperatures are typically 4 to 6°C higher than air temperatures [*Powell et al.*, 1988]. This generally good comparison between air and ground surface temperatures serves as a second check on our calculated gradients, although the difference between air and ground temperatures within geothermal areas may be higher than average because of the heat being conducted to the ground surface.

[30] Total conductive heat output for each thermal area was computed using the sequential Gaussian simulation (sGs) algorithm by the program sgsim within the geostatistical software GSLIB [*Deutsch and Journel*, 1998]. Details of the application of sGs simulations to CO_2 flux data have been described in detail by *Cardellini et al.* [2003]. For the OPTA simulations, the areas representing the nine thermal pools were removed as the heat flux from these features are calculated separately. Because the background temperature gradients in the low-permeability cap layers in vapor dominated areas are not well known, we chose a value of 1°C·m^{-1} which roughly coincides with the unforested area. Below, in this section we examine the effect of this selection.

[31] Data were declustered and a normal-score data transformation [*Deutsch and Journel*, 1998] was performed on the data from both OPTA and SPTA. Experimental variograms were computed based on the normal score data, modeled for each data set, and the variogram model was used in the sGs procedure to create 300 realizations of the temperature gradient grid. Simulations were performed using a 5-m grid spacing for each thermal area. The resulting heat flux maps for the OPTA (Figure 10) and the SPTA (Figure 11) and the histograms of diurnally corrected temperature gradients (Figure 9) suggest that areas of high conductive heat flux are localized. Assuming that the bulk thermal conductivity (1.27 ± 0.21 W·m^{-1}·K^{-1}) is uniform across both thermal areas, the conductive heat outputs from soils in the OPTA and the SPTA are 3.6 ± 0.4 MW and 7.5 ± 0.4 MW, respectively. The calculated standard

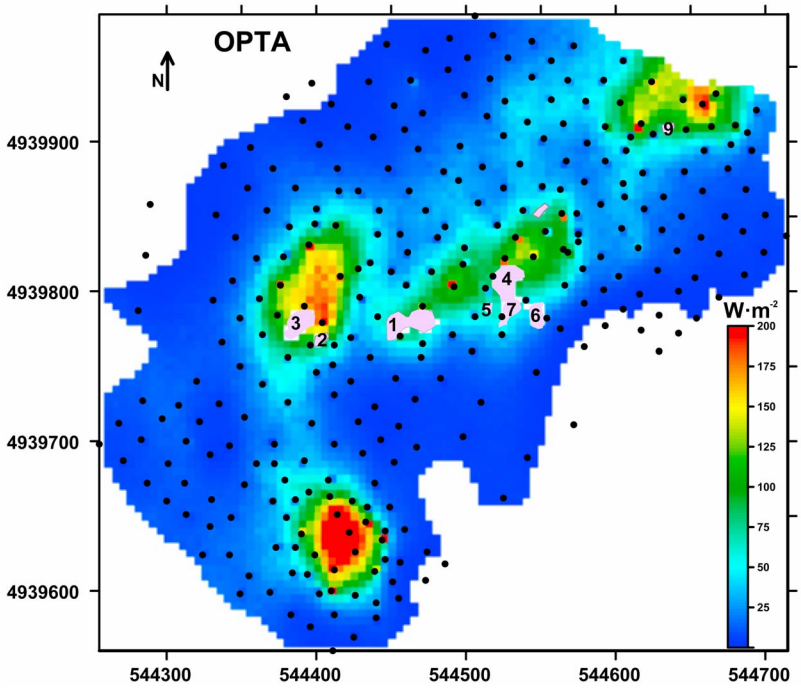

Figure 10. Map showing conductive heat flux distribution in the Obsidian Pool Thermal Area (OPTA) bounded by a temperature gradient of $1°C·m^{-1}$. The black dots represent the locations of temperature-depth measurements and the pink patches and numbers represent pool locations. Pool areas were not included in the conductive heat flux calculations or in the interpolations.

deviations result from spatial averaging of the temperature gradients and from the variability associated with the thermal conductivity determinations.

[32] The highest surface heat flux values trend approximately SW-NE in the OPTA (Figure 10) and approximately N-S in the SPTA (Figure 11) and are aligned parallel to mapped faults adjacent to each of the thermal areas [*Christiansen*, 2001]. If we assume that the base of the cap layer where the vapor is condensing is approximately isothermal, variations in conductive heat flow likely reflect variations in the thickness of the layer (Figure 5). The high heat flux toward the center of each field may indicate a thinner cap that parallels the tectonic trends or a more permeable cap where heat is transferred to the surface more efficiently.

[33] In the conductive heat flux calculations presented above we assumed a background value of $1°C·m^{-1}$, mainly based on a correlation with the areas that have no tree growth. However, this criterion might not apply to other vapor dominated areas and therefore, we calculate the conductive heat output from the OPTA and the SPTA as a function of the minimum (background) temperature gradient delimiting the thermal areas. We increase the background temperature gradient from $1°C·m^{-1}$ to $10°C·m^{-1}$ at increments of $1°C·m^{-1}$ and show that although the size of the thermal areas decrease by 43% and 15% in the OPTA and SPTA respectively, the conductive heat output decreases only by 9% in the OPTA and by 4% in the SPTA (Figure 12).

6.2. Advective Heat Flux Through Soils

[34] The average vapor flux (dm_{des}/dt) for each experiment and the standard deviation are presented in Table 2. In

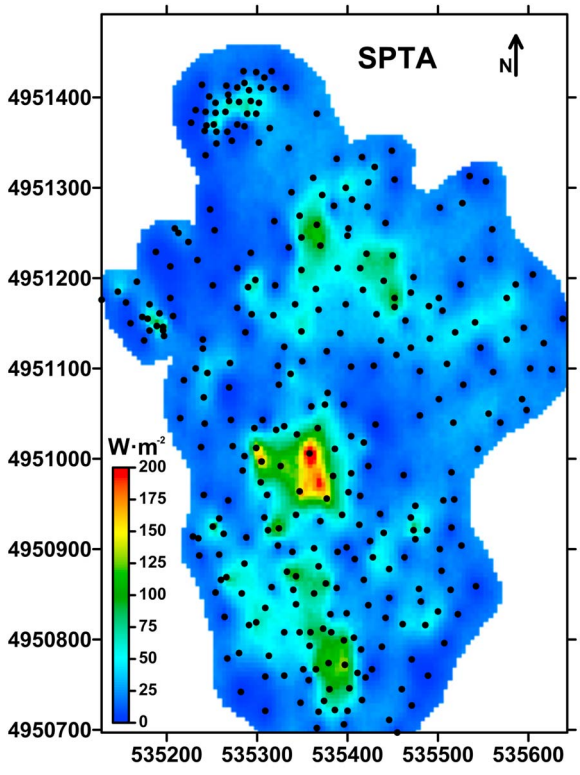

Figure 11. Map showing conductive heat flux distribution in the Solfatara Plateau Thermal Area (SPTA) bounded by a temperature gradient of $1°C·m^{-1}$. The black dots represent the locations of temperature-depth measurements.

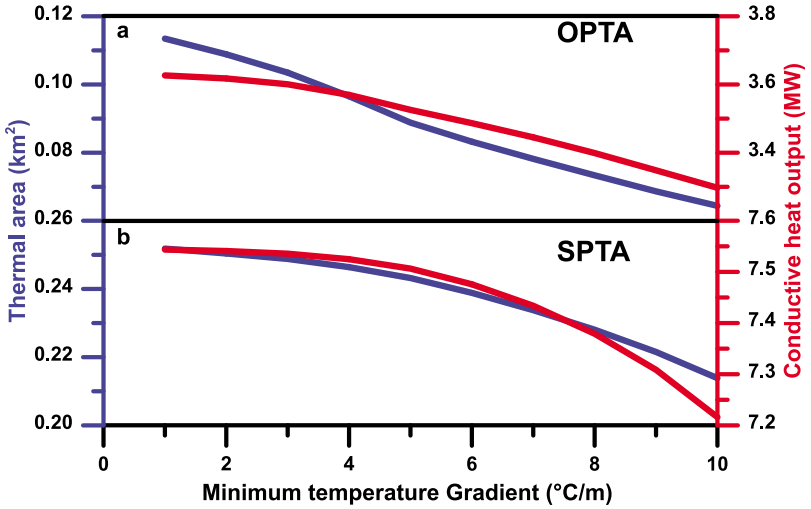

Figure 12. Variation of thermal area (blue curves) and conductive heat output (red curves) as a function of the background temperature gradient used to define the thermal area for (a) the Obsidian Pool Thermal Area (OPTA) and (b) the Solfatara Plateau Thermal Area (SPTA).

the three overnight experiments (>30 h) vapor flux was significantly less than in the shorter experiments (<6 h). The relatively low vapor flow rates in the long experiments are probably a consequence of the desiccant layer closest to the ground surface being partially saturated or cemented (and clogging vapor pathways) when the container was not shaken throughout the night. In one experiment (SP11–06) the desiccant saturated within approximately 4 h. The average water flux in all 17 experiments is 137 ± 32 $g \cdot hr^{-1} \cdot m^{-2}$ and excluding the three overnight experiments the average is 154 ± 35 $g \cdot hr^{-1} \cdot m^{-2}$. The averages at the OPTA (160 ± 66; n = 6) and the SPTA (149 ± 55; n = 8) are within error, so in the analysis below we use the combined average from the two thermal areas.

[35] The experiments with the highest vapor flow rates (OBS145, OBS146, SP11–02, and SP11–06) are associated with the highest temperature gradients (Table 2). However, in lower gradient experiments there is no straightforward correlation between thermal gradient and vapor flow rate.

[36] The time-variation of vapor temperature between the desiccant container and the ground surface, the ambient air temperature, and the subsurface temperatures in experiments SP11–02 and SP11–07 are presented in Figure 13. In experiment SP11–07 the temperature at 70 cm was 81°C and the average vapor temperature between the desiccant container and the ground surface was 46°C, which is equivalent to the temperature between 10 and 20 cm during the first part of the experiment and less than the temperature at 10 cm during the second half of the experiment (Figure 13a). In experiment SP11–02 the boiling temperature (~92°C) was measured by sensors at depths of ≥20 cm and vapor temperature fluctuated with an average of 56°C. Vapor temperature between the desiccant container and the ground surface was 20–25°C colder than the temperature at a depth of 10 cm (Figure 13b), possibly caused by entrainment of ambient air in the upper few centimeters of the soil. A strong wind between 13:45 and 14:30 MST resulted in rapid temperature fluctuations. These results indicate that the ascending vapor has cooled from boiling temperature within the low-permeability cap layer and that advective heat is transported to the surface by evaporation, consistent with theory of heat transport in partially saturated soils [*Parlange et al.*, 1998].

[37] The advective heat flux is calculated by solving equation (18) and assuming a uniform vapor flux of 154 ± 35 $g \cdot hr^{-1} \cdot m^{-2}$ (excluding the three overnight experiments) in the areas delimited by a temperature gradient of $>60°C \cdot m^{-1}$. Based on the limited measurement that we made, we chose this threshold, because high vapor flux appears to occur in areas of elevated thermal gradients. The size of the areas delimited by a temperature gradient of $>60°C \cdot m^{-1}$ and the calculated advective heat output are 13,550 m^2 and 1.3 ± 0.3 MW at the OPTA and 12,900 m^2 and 1.2 ± 0.3 MW at the SPTA. Future studies need to better quantify the relation between advective heat flux and temperature gradients in these vapor dominated areas.

6.3. Heat Flux From Thermal Pools

[38] Calculated heat output from the nine pools in the OPTA and the values of parameters used for solving equations (5)–(9) are presented in Table 1. The pools are located along an approximate northeast trend and coincide with areas of high conductive heat flux (Figure 10). The total heat output from the nine pools is 6.8 ± 1.4 MW with pools 1, 3, 4, and 5 (Figure 2) combining for 90% of the total output. Although the nine pools cover only ~1% of the OPTA area, their heat output is more than double the conductive heat flux. The evaporative component of heat flux from the pools (equation (5)) is the largest (73%) and its proportion increases with increasing pool temperature.

[39] The calculations used to derive the heat output estimates are empirical and incorporate several parameters and assumptions that are not well constrained and thus we assume a conservative error of 20%. This assumed error incorporates the variation in hourly wind speeds, barometric pressure and air temperature measured at a weather station 7.5 km away from OPTA (Figure 1), error in area determination of pool surface area, pool temperatures, and the range of assumptions

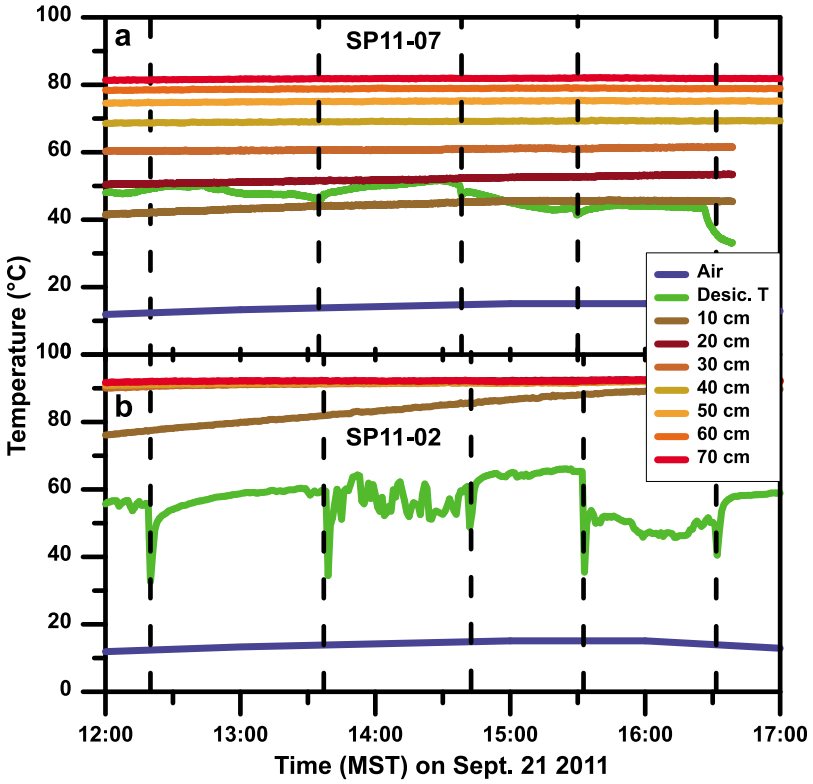

Figure 13. Time variation of temperature measurements carried out in conjunction with the soil water flux experiments at (a) SP11–07 and (b) SP11–02 in the Solfatara Plateau Thermal Area (Figure 3) in September, 2011. The blue curves are for air temperature at a weather station near Yellowstone Lake (Figure 1) and the green curves are for vapor temperature between the desiccant and the ground surface. Vertical dashed lines are for times when the desiccant boxes were removed and weighed. All other curves represent subsurface temperatures at various depths.

and parameters incorporated in equations (5)–(9). For comparison, if we insert into equation (6) the average hourly wind speed at the National Weather Service station at Old Faithful (COOP ID 486845), 35 km WSW of the OPTA; at an elevation of 2245 m (1.3 $m \cdot sec^{-1}$), the total heat output decreases by 12%. We further assume that pool temperatures do not vary with time despite the extreme air temperature variations in the YPVF, implying that heat input and output from the pools is in a steady state. We also assume evaporation of pure water although some of the low pH pools have high concentrations of clays (mud pots) and a high ionic strength.

7. Discussion

7.1. Total Heat Output

[40] We measured and quantified mechanisms and rates of near-surface heat transport in two vapor dominated, acid-sulfate thermal areas in the Yellowstone Plateau Volcanic Field (YPVF). In the OPTA and the SPTA the conductive heat output is greater than the advective output from soils and in the OPTA heat output from several thermal pools is approximately double the conductive output, even though the pools cover only 1% of the thermal area (Table 3). The calculated average vapor flux from soils, 154 ± 35 $g \cdot hr^{-1} \cdot m^{-2}$ (Table 2) that are based on the novel experiments we developed in this study are within the range measured using different methods; 54–612 $g \cdot hr^{-1} \cdot m^{-2}$ measured in Wairakei, New Zealand with a water calorimeter [*Hochstein and Bromley*, 2005], and 28–467 $g \cdot hr^{-1} \cdot m^{-2}$ measured at La Solfatara Volcano, Phlegrean Fields, Italy with a eddy covariance tower [*Werner et al.*, 2006].

[41] The total heat outputs correspond to average heat fluxes of 103 ± 2 $W \cdot m^{-2}$ and 35 ± 3 $W \cdot m^{-2}$ for the OPTA and SPTA, respectively (Table 3). These fluxes are more than an order of magnitude greater than the average heat fluxes from the Yellowstone Caldera as a whole (2.3 $W \cdot m^{-2}$) [*Fournier*, 1989] and the caldera section of Yellowstone

Table 3. Summary of Heat Output ($\dot{Q}_{cond}$) and Average Heat Flux (q*ave*) From the OPTA and the SPTA

	Area (km^2)	$\dot{Q}_{cond}$ (MW)	$\dot{Q}_{adv}$ (MW)	$\dot{Q}_{pool}$ (MW)	$\dot{Q}_{total}$ (MW)	q_{ave} ($W \cdot m^{-2}$)	Extrapolated[a] (MW)
OPTA	0.11	3.6 ± 0.4	1.3 ± 0.3	6.8 ± 1.4	11.8 ± 1.4	103 ± 2	3,600
SPTA	0.25	7.5 ± 0.4	1.2 ± 0.3	–	8.8 ± 0.4	35 ± 3	1,220

[a] q_{total} extrapolated to the 35 km^2 of vapor dominated areas in the YPVF.

Lake (1.5–2.0 $W \cdot m^{-2}$) [*Morgan et al.*, 1977; *Smith and Blackwell*, 2000; *Negraru and Blackwell*, 2004]. Heat flux in the OPTA is lower than in Hot Spring Basin, probably the hottest basin in the YPVF, located just outside the eastern margin of the caldera (Figure 1), where heat flux estimates are 140 to 370 $W \cdot m^{-2}$ over 1 km^2 [*Werner et al.*, 2008].

[42] To put these numbers in context it is important to note that many assumptions, simplifications, and uncertainties are associated with the above heat flux calculations. For example, heat flux variations in response to the large seasonal weather fluctuations in the YPVF were not considered, the advective heat flux experiments were limited in duration and areal coverage, and many assumptions and simplifications were incorporated in the calculation of heat flux from thermal pools. Our heat output estimates also do not include heat discharged through fumaroles, but visual observations that we made in June and July, 2010 at the OPTA and SPTA suggest that they are likely insignificant. In other areas of the YPVF such as Hot Springs Basin (Figure 1) where fumarolic discharge is vigorous [*Werner et al.*, 2008], advective heat flow through fumaroles might be a significant component of the total heat budget. In spite of these simplifications and uncertainties our numbers represent the first assessment of heat flux through these vapor dominated areas.

7.2. Relation to Geological Structures

[43] Results from this study show that the conductive heat flux in the OPTA and in the SPTA is focused through relatively small areas (Figures 10 and 11). In areas of very high temperature gradients, the boiling occurs at depths of less than 1 m, probably suggesting a thin or fractured "cap layer" (Figure 5). The roughly ENE trend of the elevated gradients in the OPTA (Figure 10) parallels the trend of the Elephant Back fault system [*Christiansen*, 2001]. The northernmost mapped fault lies just to the south of OPTA, but within spatial resolution limitations, many of the 1978 earthquakes were located in and around the OPTA [*Pitt and Hutchinson*, 1982]. The earthquake swarm caused a large spike in heat and CO_2 output in the Mud Volcano area within less than 1 year [*Pitt and Hutchinson*, 1982; *Evans et al.*, 2010]. The roughly N-S trend of elevated gradients in the SPTA (Figure 11) follows a series of north and northwest trending faults south of SPTA [*Christiansen*, 2001] and the general trend of normal faults inferred from the earthquake sequence of June 1975 [*Pitt et al.*, 1979]. This link between focused thermal activity and faulting suggests that either these faults serve as discontinuities along which the acid fluids dissolve the rocks forming permeable flow channels, or that these faults are active and form the permeable pathways to the surface.

7.3. Implications for Yellowstone's Heat Budget

[44] Our study covered an area of only ~1% of the ~35 km^2 of vapor dominated, acid-sulfate areas in the Yellowstone Caldera [*Rodman et al.*, 1996; *Werner and Brantley*, 2003]. Any attempt to extrapolate the calculated heat flux from the OPTA or the SPTA to larger areas is challenging, because near-surface heat flux within the thermal areas (Figures 10 and 11) and within the caldera is heterogeneous and the boundaries of thermal areas are not well defined (Figure 12). We follow the approach of *Werner and Brantley* [2003] who extrapolated soil diffuse CO_2 flux measurements from limited thermal areas to the ~35 km^2 of thermally active vapor dominated, acid-sulfate areas in Yellowstone. Extrapolation of the average heat flux from the OPTA (103 ± 2 $W \cdot m^{-2}$) to the ~35 km^2 of vapor dominated, acid-sulfate areas in the YPVF (Figure 1) amounts to 3.6 GW, which is slightly lower than the calculated range of the total heat output transported by steam from the entire YPVF using the chloride inventory method (4.0–8.0 GW). Extrapolation of the average heat flux from the SPTA (35 ± 3 $W \cdot m^{-2}$) to the ~35 km^2 of vapor dominated areas would amount to only 1.2 GW, significantly less than the total heat output transported by steam from the YPVF. The low values of extrapolated heat output from the SPTA, and to a lesser extent from the OPTA, might suggest that either the heat fluxes from the SPTA and the OPTA are not representative of the ~35 km^2 of vapor dominated areas, or that the chloride inventory method does not provide a correct estimate of total heat output from the Yellowstone magmatic system. It might also suggest that a significant amount of heat is transported (without chloride) by recharging meteoric water. The large uncertainties associated with the heat flux estimates and the large gaps in the thermal budget limit our ability to use heat as a tracer to constrain deep processes in Yellowstone's magmatic system.

7.4. Future Studies

[45] There are significant challenges in quantifying the total heat output from the YPVF that result from the great size of the underlying magmatic system, the wide distribution of thermal features, the complex interplay between the heat transport processes, the heterogeneous heat flux at many spatial scales, the large temporal variations, the large diurnal and seasonal variations of air temperature and pressure, and the involvement of multicomponent fluids. To overcome some of these challenges, labor intensive time-dependent temperature measurements are required at high spatial resolution. Because this is a daunting challenge, future studies aiming to quantify thermal changes in Yellowstone will likely be based on aerial [*Jaworowski et al.*, 2010; *Neale et al.*, 2011] or satellite [*Watson et al.*, 2008; *Vaughan et al.*, 2010; *Savage et al.*, 2012; *Vaughan et al.*, 2012] remote sensing methods. Quantification of remotely sensed heat flux estimates that are based on the thermal structure of the ground surface and the amount of heat that is radiated into the atmosphere need to rely on ground based measurements that calibrate these techniques and characterize and quantify subsurface heat transport mechanisms and rates. Recent satellite based thermal infrared estimates of radiant heat output from the YPVF (2 GW) are lower than those estimated with the chloride-inventory method and with estimates based on extrapolations from this study and are discussed in *Vaughan et al.* [2012].

[46] Our results demonstrate that the evaporative heat flux from small thermal pools in vapor dominated areas is significant and future studies should better characterize and quantify the physics of evaporation from bubbling pools containing high concentrations of clay (mud pots) and having high ionic strength as well as quantifying temporal temperature variations. Similarly, the significance of heat discharged through fumaroles is not known and could be significant in some thermal areas [*Hochstein and Bromley*, 2001].

[47] Future studies will also need to better characterize the relation between heat and multicomponent mass transfer in the variably saturated shallow subsurface of vapor dominated areas. These studies should focus on the time-dependent interplay between climate (air temperature, pressure, and moisture), water content in the shallow subsurface, the flow of water vapor and non-condensable gases, heat conduction, and evaporation to the atmosphere [*Bittelli et al.*, 2008; *Heitman et al.*, 2008]. An improved understanding of these processes in areas of high heat flux may also have implications for geothermal resource exploration.

[48] Several studies have documented changes to thermal features in Yellowstone following local and distant earthquakes. Because of the low rates of water discharge in vapor dominated areas, documentation of earthquake-induced changes in thermal activity is lacking. For example it is unknown if the 1975 Central Plateau earthquake swarms near the SPTA [*Pitt et al.*, 1979] or the 1978 Mud Volcano earthquake swarm [*Pitt and Hutchinson*, 1982] have resulted in significant heat flux changes in the SPTA and the OPTA. Additionally, the effects of the 2008–2009 Yellowstone Lake earthquake swarm that occurred ~10 km south of OPTA [*Farrell et al.*, 2010] on thermal activity are unknown. Thus, the validity of steady state heat flux assumptions in quantifying heat output from Yellowstone is questionable.

8. Conclusions

[49] On the basis of this study we conclude the following:

[50] 1. Heat transfer through a thin, clay-rich, low permeability layer capping large vapor reservoirs in the 0.11 km^2 Obsidian Pool Thermal Area (OPTA) and the 0.25 km^2 Solfatara Plateau Thermal Area (SPTA) is dominated by conduction through the solid phase, advection by vapor flow, and evaporation from several thermal pools in the OPTA.

[51] 2. The conductive heat output from the OPTA and the SPTA is 3.6 ± 0.4 MW and 7.5 ± 0.4 MW respectively. The advective heat output from the OPTA is 1.3 ± 0.3 MW and from the SPTA it is 1.2 ± 0.3 MW. Heat output from pools in the OPTA is 6.8 ± 1.4 MW. The total heat output is 11.8 ± 1.4 MW and 8.8 ± 0.4 MW from the OPTA and the SPTA, respectively.

[52] 3. Extrapolation of the average heat flux from the OPTA (103 ± 2 $W \cdot m^{-2}$) to the ~35 km^2 of vapor dominated, acid-sulfate areas in the Yellowstone Plateau Volcanic Field (YPVF) amounts to 3.6 GW, which together with the advective heat discharge through hot springs in Yellowstone (~0.6–0.8 GW) and heat transported with CO_2 (0.3 GW) is slightly lower than the calculated range of the total heat output from the YPVF (4.6–9.1 GW). Extrapolation of the average heat flux from the SPTA (35 ± 3 $W \cdot m^{-2}$) to the ~35 km^2 of vapor dominated, acid-sulfate areas combined with the advective heat discharge through hot springs and heat transported with CO_2 amounts to only 1.2 GW, which is significantly less than the estimated heat output from the YPVF.

[53] 4. The large uncertainties associated with the heat flux estimates and the large gaps in the thermal budget limit our ability to use heat as a tracer to constrain deep processes in Yellowstone's magmatic system.

[54] 5. Focused areas of high heat flux in the OPTA and the SPTA are roughly parallel to regional faults mapped outside the thermal areas, suggesting that faults serve as flow channels for the rising acid vapors.

[55] **Acknowledgments.** We thank Tori Klettke and Tim Brown for their extensive field and laboratory work that was supported by an internship through the National Association of Geoscience Teachers (NAGT) and U.S. Geological Survey (USGS) Cooperative Summer Field Training Program. Additional field work was carried out by Patrick Fulton, Russell Rosenburg, Michael Davis, Angela Diefenbach, and Greg Vaughan. Fred Grubb (USGS) carried out the thermal conductivity measurements and Dave Stonestrom (USGS) guided the porosity and water saturation measurements. Christie Hendrix and Stacy Gunther (Yellowstone National Park) assisted with coordination and logistics and Hank Heasler (Yellowstone National Park) provided aerial photos. We thank Jake Lowenstern, Greg Vaughan, and two anonymous reviewers for helpful comments. S. Hurwitz, C.A. Werner, and F. Murphy were supported by the USGS Volcano Hazards Program and R.N. Harris was supported by NSF-EAR0545342.

References

Adams, E., D. Cosler, and K. Helfrich (1990), Evaporation From heated water bodies: Predicting combined forced plus free convection, *Water Resour. Res.*, *26*, 425–435, doi:10.1029/WR026i003p00425.

Bergfeld, D., J. B. Lowenstern, A. G. Hunt, W. C. Shanks III, and W. C. Evans (2011), Gas and isotope chemistry of thermal features in Yellowstone National Park, *U.S. Geol. Surv. Sci. Invest. Rep.*, *2011–5012*, 26 pp.

Bevington, P. R. (1969), *Data Reduction and Error Analysis for the Physical Sciences*, McGraw-Hill, New York, doi:10.1119/1.17439

Bittelli, M., F. Ventura, G. S. Campbell, R. L. Snyder, F. Gallegati, and P. R. Pisa (2008), Coupling of heat, water vapor, and liquid water fluxes to compute evaporation in bare soils, *J. Hydrol.*, *362*, 191–205, doi:10.1016/j.jhydrol.2008.08.014.

Blackwell, D. D., and M. Richards (2004), Geothermal map of North America, 1 sheet, scale 1:6,500,000, Am. Assoc. of Pet. Geol., Tulsa, Okla.

Brombach, T., J. C. Hunziker, G. Chiodini, C. Cardellini, and L. Marini (2001), Soil diffuse degassing and thermal energy fluxes from the southern Lakki plain, Nisyros (Greece), *Geophys. Res. Lett.*, *28*, 69–72, doi:10.1029/2000GL008543.

Bromley, C., S. M. van Manen, and W. Mannington (2011), Heat flux from steaming ground: Reducing uncertainties, paper presented at Thirty-Sixth Workshop on Geothermal Reservoir Engineering, Stanford Univ., Stanford, Calif.

Brown, G., H. Rymer, and D. Stevenson (1991), Volcano monitoring by microgravity and energy budget analysis, *J. Geol. Soc.*, *148*, 585–593, doi:10.1144/gsjgs.148.3.0585.

Cardellini, C., G. Chiodini, and F. Frondini (2003), Application of stochastic simulation to CO_2 flux from soil: Mapping and quantification of gas release, *J. Geophys. Res.*, *108*(B9), 2425, doi:10.1029/2002JB002165.

Carslaw, H. S., and J. C. Jaeger (1959), *Conduction of Heat in Solids*, 2nd ed., Oxford Univ. Press, London.

Chang, W., R. B. Smith, C. Wicks, C. Puskas, and J. Farrell, (2007), Accelerated uplift and source models of the Yellowstone caldera, 2004–2006, from GPS and InSAR observations, *Science*, *318*, 952–956, doi:1126/science.1146842.

Chiodini, G., F. Frondini, C. Cardellini, D. Granieri, L. Marini, and G. Ventura (2001), CO_2 degassing and energy release at Solfatara volcano, Campi Flegrei, Italy, *J. Geophys. Res.*, *106*, 16,213–16,221, doi:10.1029/2001JB000246.

Chiodini, G., D. Granieri, R. Avino, S. Caliro, A. Costa, and C. Werner (2005), Carbon dioxide diffuse degassing and estimation of heat release from volcanic and hydrothermal systems, *J. Geophys. Res.*, *110*, B08204, doi:10.1029/2004JB003542.

Christiansen, R. L. (2001), The Quaternary and Pliocene Yellowstone Plateau volcanic field of Wyoming, Idaho, and Montana, *U.S. Geol. Surv. Prof. Pap.*, *729-G*, 145 pp.

Chu, R., D. V. Helmberger, D. Sun, J. M. Jackson, and L. Zhu (2010), Mushy magma beneath Yellowstone, *Geophys. Res. Lett.*, *37*, L01306, doi:10.1029/2009GL041656.

Dawson, G. B., and D. J. Dickinson (1970), Heat flow studies in thermal areas of the North Island of New Zealand, *Geothermics*, *2*, 466–473, doi:10.1016/0375-6505(70)90045-3.

Deutsch, C. V., and A. G. Journel (1998), *GSLIB: Geostatistical Software Library and Users Guide*, 369 pp., Oxford Univ. Press, New York.

Evans, W. C., D. Bergfeld, J. P. McGeehin, J. C. King, and H. Heasler (2010), Tree-ring ^{14}C links seismic swarm to CO_2 spike at Yellowstone, USA, *Geology*, *38*, 1075–1078, doi:10.1130/G31345.1.

Farrell, J., R. B. Smith, T. Taira, W.-L. Chang, and C. M. Puskas (2010), Dynamics and rapid migration of the energetic 2008–2009 Yellowstone Lake earthquake swarm, *Geophys. Res. Lett.*, *37*, L19305, doi:10.1029/2010GL044605.

Fournier, N., F. Witham, M. Moreau-Fournier, and L. Bardou (2009), Boiling Lake of Dominica, West Indies: High-temperature volcanic crater lake dynamics, *J. Geophys. Res.*, *114*, B02203, doi:10.1029/2008JB005773.

Fournier, R. O. (1979), Geochemical and hydrologic considerations and the use of enthalpy-chloride diagrams in the prediction of underground conditions in hot-spring systems, *J. Volcanol. Geotherm. Res.*, *5*, 1–16, doi:10.1016/0377-0273(79)90029-5.

Fournier, R. O. (1989), Geochemistry and dynamics of the Yellowstone National Park hydrothermal system, *Annu. Rev. Earth Planet. Sci.*, *17*, 13–53, doi:10.1146/annurev.ea.17.050189.000305.

Fournier, R. O., D. E. White, and A. H. Truesdell (1976), Convective heat flow in Yellowstone National Park, paper presented at 2nd Symposium on the Development and Use of Geothermal Resources, United Nations, San Francisco, Calif.

Fridriksson, T., B. R. Kristjánsson, H. Ármannsson, E. Margrétardóttir, S. Ólafsdóttir, and G. Chiodini (2006), CO_2 emissions and heat flow through soil, fumaroles, and steam heated mud pools at the Reykjanes geothermal area, SW Iceland, *Appl. Geochem.*, *21*, 1551–1569, doi:10.1016/j.apgeochem.2006.04.006.

Friedman, I., and D. R. Norton (2007), Is Yellowstone losing its steam? Chloride flux out of Yellowstone National Park, in *Integrated Geoscience Studies in the Greater Yellowstone Area: Volcanic, Hydrothermal and Tectonic Processes in the Yellowstone Geoecosystem*, edited by L. A. Morgan, *U.S. Geol. Surv. Prof. Pap.*, *1717*, 271–297.

Haar, L., J. S. Gallagher, and G. S. Kelt (1984), *NBS/NRC Steam Tables*, 320 pp., Hemisphere, New York.

Heasler, H. P., C. Jaworowski, and D. Foley (2009), Geothermal systems and monitoring hydrothermal features, in *Geological Monitoring*, edited by R. Young and L. Norby, pp. 105–140, Geol. Soc. of Am., Boulder, Colo.

Heitman, J. L., X. Xiao, R. Horton, and T. J. Sauer (2008), Sensible heat measurements indicating depth and magnitude of subsurface soil water evaporation, *Water Resour. Res.*, *44*, W00D05, doi:10.1029/2008WR006961.

Hochstein, M. P., and C. J. Bromley (2001), Steam cloud characteristics and heat output of fumaroles, *Geothermics*, *30*, 547–559, doi:10.1016/S0375-6505(01)00012-8.

Hochstein, M. P., and C. J. Bromley (2005), Measurement of heat flux from steaming ground, *Geothermics*, *34*, 133–160.

Hurwitz, S., J. B. Lowenstern, and H. Heasler (2007), Spatial and temporal geochemical trends in the hydrothermal system of Yellowstone National Park: Inferences from river solute fluxes, *J. Volcanol. Geotherm. Res.*, *162*, 149–171, doi:10.1016/j.jvolgeores.2007.01.003.

Hurwitz, S., W. C. Evans, and J. B. Lowenstern (2010), River solute fluxes reflecting active hydrothermal chemical weathering of the Yellowstone Plateau Volcanic Field, USA, *Chem. Geol.*, *276*, 331–343, doi:10.1016/j.chemgeo.2010.07.001.

Husen, S., R. B. Smith, and G. P. Waite (2004), Evidence for gas and magmatic sources beneath the Yellowstone volcanic field from seismic tomographic imaging, *J. Volcanol. Geotherm. Res.*, *131*, 397–410, doi:10.1016/S0377-0273(03)00416-5.

Jaupart, C., and J.-C. Mareschal (2007), Heat flow and thermal structure of the lithosphere, in *Treatise on Geophysics*, vol. 6, *Crustal and Lithosphere Dynamics*, edited by G. Schubert, pp. 217–252, Elsevier, Oxford.

Jaworowski, C., H. Heasler, C. M. U. Neale, and S. Sivarajan (2010), Using thermal infrared imagery and LiDAR in Yellowstone geyser basins, *Yellowstone Sci.*, *18*, 8–19.

Jorand, R., A. Fehr, A. Koch, and C. Clauser (2011), Study of the variation of thermal conductivity with water saturation using nuclear magnetic resonance, *J. Geophys. Res.*, *116*, B08208, doi:10.1029/2010JB007734.

Lowenstern, J. B., and S. Hurwitz (2008), Monitoring a supervolcano in repose: Heat and volatile flux at the Yellowstone Caldera, *Elements*, *4*, 35–40, doi:10.2113/GSELEMENTS.4.1.35.

Lowenstern, J. B., R. B. Smith, and D. P. Hill (2006), Monitoring supervolcanoes: Geophysical and geochemical signals at Yellowstone and other caldera systems, *Philos. Trans. R. Soc. A*, *364*, 2055–2072, doi:10.1098/rsta.2006.1813.

Lowenstern, J. B., D. Bergfeld, W. C. Evans, and S. Hurwitz (2012), Generation and evolution of hydrothermal fluids at Yellowstone: Insights from the Heart Lake Geyser Basin, *Geochem. Geophys. Geosyst.*, *13*, Q01017, doi:10.1029/2011GC003835.

Morgan, P., D. D. Blackwell, R. E. Spafford, and R. B. Smith (1977), Heat flow measurements in Yellowstone Lake and the thermal structure of the Yellowstone Caldera, *J. Geophys. Res.*, *82*, 3719–3732, doi:10.1029/JB082i026p03719.

Neale, C. M. U., S. Sivarajan, A. Masih, C. Jaworowski, and H. Heasler (2011), Estimating heat flow of thermal features in Yellowstone National Park using airborne thermal infrared remote sensing, Abstract H51C-1225 presented at 2011 Fall Meeting, AGU, San Francisco, Calif., 5–9 Dec.

Negraru, P. T., and D. D. Blackwell (2004), Interpretation of heat flow and seismic data from Yellowstone Lake, Yellowstone National Park, *Eos Trans. AGU*, *85*(47), Fall Meet. Suppl., Abstract T43B-1322.

Newhall, C. G., and D. Dzurisin (1988), Historical unrest at large calderas of the world, *U.S. Geol. Surv. Bull.*, *1855*, 1108 pp.

Parlange, M. B., A. T. Cahill, D. R. Nielsen, J. W. Hopmans, and O. Wendroth (1998), Review of heat and water movement in field soils, *Soil Tillage Res.*, *47*, 5–10, doi:10.1016/S0167-1987(98)00066-X.

Pasternack, G. B., and J. C. Varekamp (1997), Volcanic lake systematics. I: Physical constraints, *Bull. Volcanol.*, *58*, 528–538, doi:10.1007/s004450050160.

Pelton, J. R., and R. B. Smith (1979), Recent crustal uplift in Yellowstone National Park, *Science*, *206*, 1179–1182, doi:10.1126/science.206.4423.1179.

Pierce, K. L., and L. A. Morgan (2009), Is the track of the Yellowstone hotspot driven by a deep mantle plume? Review of volcanism, faulting, and uplift in light of new data, *J. Volcanol. Geotherm. Res.*, *188*, 1–25, doi:10.1016/j.jvolgeores.2009.07.009.

Pitt, A. M., and R. A. Hutchinson (1982), Hydrothermal changes related to earthquake activity at Mud Volcano, Yellowstone National Park, Wyoming, *J. Geophys. Res.*, *87*, 2762–2766, doi:10.1029/JB087iB04p02762.

Pitt, A. M., C. S. Weaver, and W. Spence (1979), The Yellowstone Park earthquake of June 30, 1975, *Seismol. Soc. Am. Bull.*, *69*, 187–205.

Powell, W. G., D. S. Chapman, N. Balling, and A. E. Beck (1988), Continental heat-flow density, in *Handbook of Terrestrial Heat Flow Density Determination*, 1st ed., edited by R. Haenel, L. Rybach, and L. Stegena, pp. 167–222, Kluwer Acad., Boston, Mass., doi:10.1007/978-94-009-2847-3_5.

Rodman, A., H. Shovic, and D. Thoma (1996), *Soils of Yellowstone National Park*, Yellowstone Cent. for Resour., Mammoth Springs, Wyo.

Sass, J. H., A. H. Lachenbruch, and R. J. Munroe (1971), Thermal conductivity of rocks from measurements on fragments and its application to heat-flow determinations, *J. Geophys. Res.*, *76*(14), 3391–3401, doi:10.1029/JB076i014p03391.

Sass, J. H., C. Stone, and R. J. Munroe (1984), Thermal conductivity determinations on solid rock—A comparison between a steady-state divided-bar apparatus and a commercial transient line-source device, *J. Volcanol. Geotherm. Res.*, *20*, 145–153, doi:10.1016/0377-0273(84)90071-4.

Savage, S. L., R. L. Lawrence, S. G. Custer, J. T. Jewett, S. L. Powell, and J. A. Shaw (2012), Analyzing change in Yellowstone's terrestrial emittance with Landsat imagery, *GISci. Remote Sens.*, *49*, 317–345, doi.org/10.2747/1548-1603.49.3.317.

Shock, E. L., M. Holland, D. R. Meyer-Dombard, and J. P. Amend (2005), Geochemical sources of energy for microbial metabolism in hydrothermal ecosystems: Obsidian Pool, Yellowstone National Park, in *Geothermal Biology and Geochemistry in Yellowstone National Park*, edited by W. P. Inskeep and T. R. McDermott, pp. 95–110, Thermal Biol. Inst., Mont. State Univ., Bozeman.

Smith, R. B., and D. D. Blackwell (2000), Heat flow and energetics of Yellowstone Lake hydrothermal systems, *Eos Trans. AGU*, *81*(48), Fall Meet. Suppl., Abstract V22F-17.

Smith, R. B., and L. W. Braile (1994), The Yellowstone hotspot, *J. Volcanol. Geotherm. Res.*, *61*, 121–187, doi:10.1016/0377-0273(94)90002-7.

Sorey, M. L., and E. M. Colvard (1994), Measurements of heat and mass flow from thermal areas in Lassen Volcanic National Park, California, 1984–93, *U.S. Geol. Surv. Water Res. Invest. Rep.*, *94-4180-A*, 35 pp.

Vaughan, R. G., L. P. Keszthelyi, A. G. Davies, D. J. Schneider, C. Jaworowski, and H. Heasler (2010), Exploring the limits of identifying sub-pixel thermal features using ASTER TIR data, *J. Volcanol. Geotherm. Res.*, *189*, 225–237, doi:10.1016/j.jvolgeores.2009.11.010.

Vaughan, R. G., L. P. Keszthelyi, J. B. Lowenstern, C. Jaworowski, and H. Heasler (2012), Use of ASTER and MODIS thermal infrared data to quantify heat flow and hydrothermal change at Yellowstone National Park, *J. Volcanol. Geotherm. Res.*, *233–234*, 72–89, doi:10.1016/j.jvolgeores.2012.04.022.

Watson, F. G. R., R. E. Lockwood, W. B. Newman, T. N. Anderson, and R. A. Garrott (2008), Development and comparison of Landsat radiometric and snowpack model inversion techniques for estimating geothermal heat flux, *Remote Sens. Environ.*, *112*, 471–481, doi:10.1016/j.rse.2007.05.010.

Werner, C., and S. Brantley (2003), CO_2 emissions from the Yellowstone volcanic system, *Geochem. Geophys. Geosyst.*, *4*(7), 1061, doi:10.1029/2002GC000473.

Werner, C., S. L. Brantley, and K. Boomer (2000), CO_2 emissions related to the Yellowstone volcanic system: 2. Statistical sampling, total degassing, and transport mechanisms, *J. Geophys. Res.*, *105*, 10,831–10,846, doi:10.1029/1999JB900331.

Werner, C., G. Chiodini, D. Granieri, S. Caliro, R. Avino, and M. Russo (2006), Eddy covariance measurements of hydrothermal heat flux at Solfatara volcano, Italy, *Earth Planet. Sci. Lett.*, *244*, 72–82, doi:10.1016/j.epsl.2006.01.044.

Werner, C., S. Hurwitz, D. Bergfeld, W. C. Evans, J. B. Lowenstern, H. Heasler, C. Jaworowski, and A. Hunt (2008), Volatile emissions and gas geochemistry of Hot Spring Basin, Yellowstone National Park, USA, *J. Volcanol. Geotherm. Res.*, *178*, 751–762, doi:10.1016/j.jvolgeores.2008.09.016.

White, D. E., L. J. P. Muffler, and A. H. Truesdell (1971), Vapor-dominated hydrothermal systems compared with hot-water systems, *Econ. Geol.*, *66*, 75–97, doi:10.2113/gsecongeo.66.1.75.

Wicks, C., W. Thatcher, D. Dzurisin, and J. Svarc (2006), Uplift, thermal unrest, and magma intrusion at Yellowstone caldera, *Nature*, *440*, 72–75, doi:10.1038/nature04507.